Heat Transfer and Film Cooling Performance on a Transonic Converging Nozzle Guide Vane Endwall With Purge Jet Cooling and Dual Cavity Slashface Leakage

Daniel Richard Van Hout

Thesis submitted to the faculty of the Virginia Polytechnic Institute and State University in partial fulfillment of the requirements for the degree of

Master of Science
In
Mechanical Engineering

Wing F. Ng, Chair
K. Todd Lowe
Changmin Son

September 15, 2020
Blacksburg, VA

Keywords: Heat Transfer, Film Cooling, Endwall, Nozzle Guide Vane, Slashface gap, Dual Cavity, Aft Cavity, Fwd Cavity, Single Cavity, Jump Cooling, Ingestion, Egression, Pressure, Turbulence, Mass Flow Ratio, Transonic, CFD

Heat Transfer and Film Cooling Performance on a Transonic Converging Nozzle Guide Vane Endwall With Purge Jet Cooling and Dual Cavity Slashface Leakage

Daniel Richard Van Hout

ABSTRACT

The following study presents an experimental and computational investigation on the effects of implementing a dual cavity slashface configuration and varying slashface coolant leakage mass flow rate on the thermal performance for a 1st stage nozzle guide vane axisymmetric converging endwall. An upstream doublet staggered cylindrical hole jet cooling scheme provides additional purged coolant with consistent conditions throughout the investigation. The effects are measured in engine representative transonic mainstream and coolant flow conditions where $M_{exit} = 0.85$, $Re_{exit} = 1.5 \times 10^6$, freestream turbulence intensity of 16%, and a coolant density ratio of 1.95.

Four combinations of slashface Fwd and Aft cavity mass flow rate are experimentally analyzed by comparing key convective heat transfer parameters. Data is collected and reduced using a combination of IR thermography and a linear regression technique to map endwall heat transfer performance throughout the passage. A flow visualization study is employed using 100 cSt oil-based paint to gather qualitative insights into the endwall flow field. A complimentary CFD study is carried out to gather additional understanding of the endwall flow ingestion and egression behavior as well as comparing performance against a conventional cavity configuration.

Experimental comparisons indicate slashface mass flow rate variations have a minor effect on passage film cooling coverage. Instead, coolant coverage across the passage is primarily driven by upstream purge coolant. However, endwall heat transfer coefficient is reduced as much as 20% in mid-passage areas as leakage flow decreases. This suggests that changes in leakage flow maintains a first order correlation in altering passage aerodynamics that, despite relatively consistent film cooling coverage, also leads to significant changes in net heat flux reduction in the passage.

Endwall flow behavior proves to be complex along the gap interface showing signs of ingestion, egression, and tangential flow varying spatially throughout the gap. CFD comparisons

suggests that a dual cavity configuration varies the gap static pressure distribution closer to the mainstream pressure throughout the passage in high speed applications compared to a single cavity configuration. The resulting decelerating flow creates a more stable endwall flow profile and favorable coolant environment by reducing boundary layer thinning and shear interaction in near gap endwall tangential flow.

Heat Transfer and Film Cooling Performance on a Transonic Converging Nozzle Guide Vane Endwall With Purge Jet Cooling and Dual Cavity Slashface Leakage

Daniel Richard Van Hout

GENERAL AUDIENCE ABSTRACT

Gas turbines are often exposed to high temperatures as they convert hot, energetic gas streams into mechanical motion. As turbines receive higher temperature gases, their efficiency increases and reduces waste. However, these temperatures can get too hot for turbine parts. To survive these high temperatures, turbine components are often assembled with a gap in between to allow the part to expand and contrast when it heats and cools. Relatively cold air is also fed into the gap to help prevent hot gases from entering. This cold air can also feed into other pathways to flow onto the turbine component's surface and act as an insulating layer to the hot gas and protect the component from overheating.

The study presented investigates an assembly gap, referred to as a slashface gap, found in the middle of a vane located immediately after gas combustion with cold air leaking through. One unique aspect of this study is that there are two pathways for cold air, or coolant, to leak through when, typically, there is only one. The slashface gap lies on a wall which the vanes are attached to, referred to as the endwall. Multiple small holes on the endwall in between the combustor and vanes jet out coolant to try and protect the endwall from hot gases. These holes, called jump cooling holes, point out towards the vanes and angled more shallowly so that the holes do not face directly up from the endwall. The holes are angled as they are meant to gracefully spray coolant to cover and insulate the endwall instead of mixing with the hot air above.

The experiments found that changing how much coolant is leaked through the slashface has little effect on how much coolant from jump cooling holes covered the endwall. However, smaller slashface leaks better protect the endwall from the hot gas by forcing it to move smoother and give off less heat across the endwall rather than a tumbling like manner. The experiment is modeled on a computer simulation to determine the differences of a slashface gap with the typical one coolant pathway and the coolant dual pathway configuration that is tested in the experiments. This simulation discovered that having two coolant pathways significantly

reduces how much hot gas and jump cooling coolant enters and leaves the slashface gap. This makes the surrounding airflow along the endwall travel more smoothly and does not give off as much heat as if a single coolant pathway configuration is used instead.

DEDICATION

I would like to dedicate my thesis work to my brother, Michael Van Hout. Without him, I would have no thesis work to write. Multiple times has he has caught me when I had no one to fall back on, pulled me up when I have fallen, and pushed me when I ran out of fuel. Never have I been so motivated than brotherly competition, and never have I been so supported for than brotherly love. He always made sure that I kept focused on the future and what I should be doing to achieve my life goals, even if said unpleasantly. He has been a mentor, a brother, and a friend whom I will in no way ever be capable of doing for him as he has done for me. May we never give the dream up.

ACKNOWLEDGEMENTS

I want to first acknowledge Dr. Wing Ng, my mentor and advisor. It has sincerely been one of the greatest honors of my life to know and work under him. He has shown me the kind of person I ought to be, and I wish to one day emulate his character. Throughout my time with him, I have always felt that he truly cared about my well-being and my personal growth. It is that leadership ability and thoughtfulness that I wish to reflect in my upcoming career as well as all aspects in life. I would not have pursued a Master's degree if it were not for Dr. Ng's belief in me, and I will forever be grateful of the opportunity he has extended me and the once-in-a-lifetime experiences I have had. I am not sure that I have fully met his hope and expectations in me, but I will carry his encouragement for excellence throughout my life in hopes to one day exceed them.

I would also like to secondly acknowledge Shuo Mao, my research partner and project student lead. He has without a doubt made this thesis possible for me. Shuo had taken me on the project, shown me ropes, and supported me in any way he could. Never have I worked directly with someone as intelligent as him. I learned countless valuable lessons from his mentorship, not only in theory and practical applications, but in professionalism, demeanor, and communication. It was truly a pleasure, and I highly appreciate the quality of his work to this project.

I would also like to acknowledge the work done by the rest of the research team for their massive contributions they have made. Kaiyuan Zhang completed all presented CFD work and was instrumental to this thesis. I am not sure how else I could have conceptualized the complexities of this study without his inclusion. Jin Woo Lee has played a key role in this project since before I joined. His invaluable dedication and yearn for the team's success had helped me stay motivated at times when my momentum was slowing. Mathew Clayton, the newest team member, assisted in much needed times, and often desired to work more than what we could offer. I also appreciate all the previous researchers on the Solar Turbines Research Project at Virginia Tech and their work that is used as the groundwork of the following study presented.

I would also like to thank my previous research partners Edward Turner and Mathew Bogdan for providing me the initial opportunity to work under them at APPL. I gained valuable experience through our projects that carried over to my graduate research that has tremendously impacted my confidence and motivation. Without their support, I would not be where I am today.

My experience working with Solar Turbines Incorporated has been an exciting opportunity as I more thoroughly studied unique gas turbine technology through experimental research. It was a pleasure communicating with Hongzhou Xu throughout the project whom I always looked forward to speaking with. I am heartfeltly appreciative of the funding Solar Turbines and those involved has provided towards my graduate studies and the opportunity to work in a fascinating field. I hope my work reflects a positive investment in me, Dr. Ng, and Virginia Tech University.

Special thanks to K. Todd. Lowe, one of my committee members, who has played a significant role in my development both as an undergraduate and graduate student. I am honored to have worked so closely under him during my studies. Dr. Lowe's consistent encouragement had aided my motivation to try my best no matter the odds, and his respectful etiquette is a trait I wish to model after. I am also honored to have Dr. Changmin Son as my other committee member whom I regret not befriending more as a mentor yet am grateful for the opportunity to have a true expert review my work. Another great honor to have was to be a student of Dr. Walter O'Brien's during his last semester of teaching. His Turbomachinery lecture was the most influential class to persuade my interests in and beyond graduate school. May he rest in peace.

I would also like to give a big acknowledgement to Randall Monk, the machinist at APPL. His fantastic problem-solving ability and expert machining skills has made a significant impact on the success of this project. His assistance in tunnel repairs, practical design and knowledge, and facility maintenance made significant easing of a difficult project. And I would like to thank Bill Songer at the ME machine shop for providing useful design feedback as well as machining the necessary components needed for the experiments. I also appreciate the good friends I have made at APPL outside of this project that have been critical in helping solve tough problems and to socialize and relax with including: Blaine Hugger, Albrey de Clerck, Mathew Ruda, Cody Dowd, Ashwin Kumar, Piyush Raj, and all of the other members of AAPL

The community at whole in Virginia Tech gave me a sense of home, and I must give recognition to the ME department staff for their support and patience and to the professors who have touched my life. Lastly, my greatest thanks to my family for providing the support that have made me who I am today. These recent times have been a reminder that family remains the most important consideration in life. I cannot express how much I appreciate the loved ones around me who have provided me the time and means so that I may pursue the dreams of life.

Table of Contents

List of Figures ..... **x**
List of Tables ..... **xi**
List of Equations ..... **xii**
Nomenclature ..... **xiii**
Introduction **1**
Relevant Past Studies **2**
Experimental Apparatus **4**
A. Virginia Tech Transonic Blowdown Wind Tunnel Facility **4**
B. Test section and Linear Cascade **6**
C. Coolant Flow Parameters Relevance and Control **9**
D. IR Thermography **10**
E. Data Post-processing approach **11**
Results and Discussion **16**
A. Preamble **16**
B. CFD Validation **17**
B. Passage Aerodynamics **22**
C. Adiabatic Film Cooling Effectiveness **29**
D. Heat Transfer Coefficient **32**
E. Net Heat Flux Reduction **35**
F. CFD: Dual vs Single Cavity **38**
Conclusions **44**
Acknowledgements **46**
References **47**
Appendix A: Remaining Completed Cases **50**
Appendix B: Mainstream Conditions Calculation **54**
Appendix C: IR Camera Calibration **55**

List of Figures

Figure 1. Example of a typical NGV component w/ seal strip insertion in the SF gap of assembled components [1] .1
Figure 2. Virginia Tech Transonic Wind Tunnel 5
Figure 3. Test section cascade w/ NGV and endwall geometry 7
Figure 4. Pitchwise view of cascade endwall profile with coolant interface geometry 8
Figure 5. CAD model of opto-mechanical assembly from the IR camera view 11
Figure 6. Example of DLRT applied on a single pixel 14
Figure 7. Computational model and mesh 18
Figure 8. CFD limiting streamlines superimposed on experimental flow visualization 20
Figure 9. CFD comparison of η and HTC distributions with baseline experimental results 21
Figure 10. Flow visualization oil paint application prior to blowdown 22
Figure 11. Entire flow visualization results for baseline case 23
Figure 12. Aft portion of flow visualization 24
Figure 13. Flow visualization results surrounding the SF gap Fwd cavity 26
Figure 14. Flow visualization results surrounding the SF gap Aft cavity 27
Figure 15. CFD SF gap spanwise velocity contour at baseline conditions 28
Figure 16. CFD SF gap tangential velocity contour at baseline conditions 29
Figure 17. Adiabatic film cooling effectiveness distribution results for baseline case 30
Figure 18. Adiabatic film cooling effectiveness distribution for all reported test cases 31
Figure 19. Heat transfer coefficient distribution results for baseline case 33
Figure 20. Heat transfer coefficient distribution for all reported test cases 34
Figure 21. Net heat flux reduction distribution results for baseline case 36
Figure 22. Net heat flux reduction distribution for all reported test cases 37
Figure 23. Computational geometry of each slashface plenum configuration 39
Figure 24. CFD comparison of endwall adiabatic film cooling effectiveness distribution 40
Figure 25. CFD comparison of endwall HTC distribution 40
Figure 26. CFD comparison of spanwise velocity along the slashface gap 41
Figure 27. Spanwise velocity of flow along the SF gap interface 42
Figure 28. Comparison of pressure along the slashface gap interface normalized to mainstream total pressure 43
Figure 29. Comparison of spanwise pressure gradient along the slashface gap interface 44
Figure 30. Adiabatic effectiveness distribution comparison between baseline case and no upstream purge coolant .50
Figure 31. Adiabatic effectiveness distribution comparison between baseline case and no slashface leakage 51
Figure 32. Heat transfer coefficient distribution comparison between baseline case and no upstream purge coolant51
Figure 33. Heat transfer coefficient distribution comparison between baseline case and no slashface leakage 52
Figure 34. Net heat flux reduction distribution comparison between baseline case and no upstream purge coolant .52
Figure 35. Net heat flux reduction distribution comparison between baseline case and slashface leakage 53
Figure 36. Example of experimental based calculation for mainstream inlet and exit Mach number plot 54
Figure 37. IR camera calibration raw data aligned plot 55
Figure 38. IR camera linear regression plot 56

List of Tables

Table 1. Mainstream flow condition 6
Table 2. Details of 1st stage NGV linear cascade 6
Table 3. Details of coolant interface geometry 8
Table 4. Experimental test matrix w/ baseline case highlighted 16
Table 5. Grid independence test results 18

List of Equations

Equation 1. Density ratio 9
Equation 2. Velocity ratio 9
Equation 3. Mass flow ratio 9
Equation 4. Cook Felderman numerical heat transfer expression 11
Equation 5. Adiabatic film cooling effectiveness for high speed turbine application 12
Equation 6. Heat transfer coefficient for the endwall surface 12
Equation 7. Linearized DLRT governing equation 13
Equation 8. Recovery temperature simplified using recovery coefficient 13
Equation 9. Net Heat Flux Reduction in applicable expression 15
Equation 10. Overall film cooling effectiveness definition 15
Equation 11. Adiabatic film cooling effectiveness used in CFD 19
Equation 12. Mainstream Mach number calculation 54

Nomenclature

A	Area
BBAR	Broad Band Anti-Reflective
C	Chord
CFD	Computational Fluid Dynamics
C_r	Recovery Coefficient
D	Diameter
DLRT	Dual Linear Regression Technique
DR	Density Ratio
Fwd	Forward
Ge	Germanium
HSV	Horseshoe Vortex
HTC	Heat Transfer Coefficient
IR	Infrared
k	Thermal Conductivity, $\frac{W}{m^2K}$
LE	Leading Edge
Ma	Mach Number
MFR	Mass Flow Ratio
NGV	Nozzle Guide Vane
NHFR	Net Heat Flux Reduction
PLV	Pressure leg vortex
PS	Pressure Side
PV	Passage Vortex
q”	Heat Flux, $\frac{W}{m^2}$
Re	Reynolds number
SF	Slashface
SF_6	Sulfur hexafluoride
SLV	Suction side leg vortex
SS	Suction Side
T	Temperature

TE	Trailing edge
Tu	Turbulence intensity
V	Velocity, $\frac{m}{s}$
VR	Velocity Ratio
x	Axial coordinate
W	Width

Greek

α_1	Jump cooling injection angle
α_2	Slashface gap angle
β_1	Vane inlet angle
β_2	Vane outlet angle
γ	Specific Heat Ratio
η	Adiabatic film cooling effectiveness
ρ	Density
φ	Overall film cooling effectiveness

Subscripts

aw	Adiabatic wall
ax	Axial direction
c	Coolant flow
r	Recovery
s	Spanswise
S	static
t	tangential
T	total
p	Perpendicular
SF	Slashface
w	Wall
∞	Mainstream flow

Introduction

As the gas turbine research community work to increase the combustion temperature in the effort to increase the efficiency and specific power, countermeasures must be taken to ensure turbine component protection. If neglected, thermal loads can lead to adolescent component failure including thermal fatigue or creep. Special considerations to vulnerable geometries must be carried out to ensure a reasonable life cycle. Immediately after the combustor lies the 1st stage nozzle guide vane (NGV) where thermal protection is required for operation as the proximity to the combustor exit guarantees the most severe flow conditions imparting heat beyond the component material threshold. While thermal coated barriers provide an insulating layer to the exposed surface, sophisticated surface cooling techniques must be used to promote component vitality.

When NGV's are manufactured for conventional gas turbine operations, they are typically casted in a 2-vane single part set. As they are assembled onto the hub assembly, there lies a small gap along the direction of the passage that allows space for component thermal expansion. Throughout this study, this gap will be referred to the slashface (SF) gap. Other common nomenclature includes platform gap, mateface gap, midpassage gap, and endwall gap. A consequence for this assembly need is the vulnerability the gap presents in hot gas ingestion. Attempts in preventing the intake of thermally dangerous gases include the installation of a seal strip that inserts in the endwall assembly interface throughout the gap. Figure 1 shows a typical casted NGV part with a seal strip installation example.

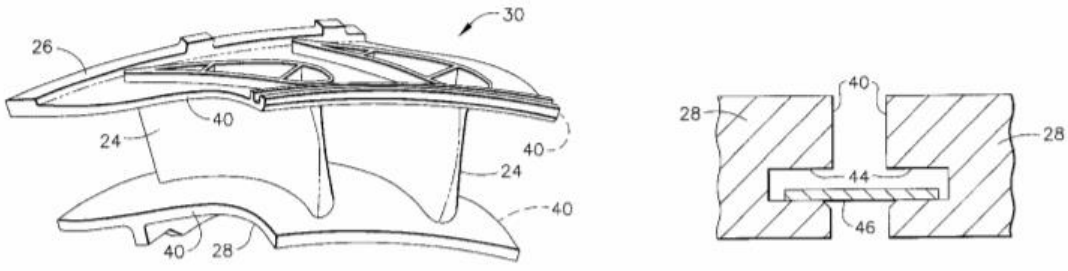

Figure 1. Example of a typical NGV component w/ seal strip insertion in the SF gap of assembled components [1]

Slashface leakage is regarded as another defense against ingestion with the idea that a pressurized cavity maintains a barrier preventing external flow through the gap. Although coolant coverage can increase with the introduction of SF leakage, it does not appear to have much success as the only source. Purge jet cooling schemes are another common and effective method in providing necessary coolant coverage on the endwall. Coolant supply is achieved using highly pressurized air from the downstream compressor that is circumvented around the combustor and fed into coolant supply interfaces through ducted networks. Largely due to the drastic increase of mainstream temperature relative to the circumvented compressed air, the density ratio of the mediums is typically near 2.

The present study examines the implementation of a unique dual cavity (plenum) slashface configuration on an engine-based 1st stage NGV endwall coupled with a purge jet cooling scheme matching engine representative density ratio. Slashface leakage rates are varied to evaluate the usefulness of a split gap design. Further details of endwall flow interactions with the SF geometry are found experimentally and computationally. A computational study is performed to better understand the effects of using a dual cavity rather than the typical single cavity SF gap.

Relevant Past Studies

The endwall flow field is critical in the development of endwall film coverage as well as other heat transfer parameters. A thorough understanding in passage secondary flows is detailed in Wang et al. [2]. A multiple smoke-wire flow visualization technique allows the observation and tracing of vortices in high-performance turbine stages. This study documents the observation of key secondary flows including the horseshoe vortex (HSV), Passage vortex (PV), the bifurcation of the HSV into both a pressure side leg vortex (PLV) and a suction side leg vortex (SLV). Smaller corner vortices at the vane wall can be found at both the trailing edge (TE) and leading edge (LE). The HSV forms from the stagnation of the incoming boundary near the LE due to the stagnation points at the LE walls. The HSV then collapses into the two smaller leg vortices where they separate to their respective side: the PLV traveling into the passage along the PS vane wall, and the SLV wrapping around the suction side (SS) vane wall. As they reach near midpassage, the passage flow sweeps the PLV across the passage towards the SS. This sweeping cross flow augments the intensity of the vortex as it forms into the PV.

Aunapu et al. [3] ran a series of experiments to modify endwall PV development by delaying the migration to the SS. One test setup used a set of 12 discrete hub endwall jets to successfully delay the PV migration. No effect on the strength of the vortex was observed. This was achieved by jetting approximately 2% of total passage flow distributed over 44% of the chord. The effect of this created an improved environment for film cooling effectiveness along the SS endwall. The effects of secondary flows on endwall heat transfer were investigated by Ames et al. [4], Blair [5], and Kang et al. [6]. These studies found typical high heat transfer locations are near the TE stagnation point and along the path of the SS horseshoe leg vortices. A location of low heat transfer is found at the region where the PV lifts during the passage crossing. More importantly, it was found that the PV swept endwall film cooling towards the SS along with its path.

Although leakage through the SF gap can maintain desired component shielding, Reid et al. [7] determined a drop of 1.5% in stage efficiency compared to a smooth endwall due to aerodynamic losses. Piggush and Simon [8] found that leakage suffers relatively drastic consequences regarding aerodynamic losses due to the addition of low-streamwise-velocity that formed a thicker boundary layer in locations with high velocity. The study also found that the passage vortex was reduced by upstream ingestion where a calculated ingested mass flow was 1.07% of the mainstream up until 0.42 C_{ax}. In the same study, Piggush and Simon observed a second vortex formed below and separate from the passage vortex from high spanwise shear. Lynch and Thole [9] expanded on the new formed vortex explaining that separation occurs due to high velocity egression. The separated flow nearly immediately reattaches due to high endwall pressure and causes high turbulence mixing and increasing heat transfer levels.

Lynch and Thole [10] concluded that the mainstream flow and upstream coolant interaction with slashface geometry is the most important performance indicator. They supplemented the use of successfully completely blocking ingestion using both a seal strip and coolant leakage. Piggush and Simon [11] report no measurable influence of the HSV due to the axisymmetric converging endwall accelerating the flow as well as upstream gap ingestion thinning the incoming boundary layer and reducing the HSV intensity. Roy et al. [12] tested a slashface gap geometry under transonic conditions in a turbine blade cascade and found that upstream coolant ingestion reduces coolant coverage on the pressure side (PS) of the endwall.

This study also concluded that coolant spread is highly dependent on relative gap location and endwall/vane design as well as coolant spread behavior being dominated by upstream coolant.

Cardwell et al. [13] concluded that the slashface gap leakage proved little effect on endwall adiabatic effectiveness levels and that it would require a significant amount of pressure to significantly affect the slashface gap velocity distribution. Chowdhury et al. [14] observed in an experimental turbine vane with slashface leakage that at much higher mass flow rates for slashface leakage coolant coming out of the upstream portion spills toward the pressure side. This observation is in concurrence with Ranson and Thole [15] where their study showed that the flow through the gap was initially directed toward the pressure side of the endwall, due to the incoming velocity vectors, then proceeding to the suction side of the endwall. Chen et al. [16] made a similar conclusion where the higher slashface leakage tends to allow more coolant coverage on the suction side endwall farther upstream.

Granser and Schulenber [17] studied the injection of fluid into boundary layers and the resulting improvement in boundary layer by reenergizing the profile due to high momentum injection hence mitigating secondary flow strength and adverse heat transfer affects. Zhang and Jaiswal [18] also illustrates high jet momentum interacting with passage secondary flows and the ensuing suppressing characteristic. Sibold [19] describes how coolant characteristics, namely density ratio, plays a significant role in coolant momentum penetrating secondary flows for accurate endwall heat transfer studies.

Experimental Apparatus

A. Virginia Tech Transonic Blowdown Wind Tunnel Facility

Measurements for endwall heat transfer and adiabatic film cooling effectiveness are obtained using the Virginia Tech Transonic Blowdown Wind Tunnel. This facility is a heated blowdown type wind tunnel including a scaled-up linear cascade test section installed downstream of a turbulence grid. The tunnel layout is displayed in Figure 2. The blowdown operation provides a maximum flow rate of 4.5 kg/s that can be sustained for up to 30 seconds through the test section allowing a quasi-steady aerodynamic flow field and transient heat transfer measurements for exit Mach numbers between 0.6 and 1.2. Supplied air originates from a 5,000-gallon tank at 1,207 kPa that is dried through an Aircell dryer to a dew point near -70 °C for minimizing moisture content during operation. Two pneumatically actuated valves control

the supplied air from the tank. A Bettis CB725-SR60 pneumatic actuator acts as a safety valve to prevent over-pressurization to the tunnel, and the Fisher DVC6200 Digital Valve Controller manipulates a butterfly valve to regulate inlet flow to a desired operating inlet pressure using a positive feedback algorithm and real-time tunnel pressure measurements.

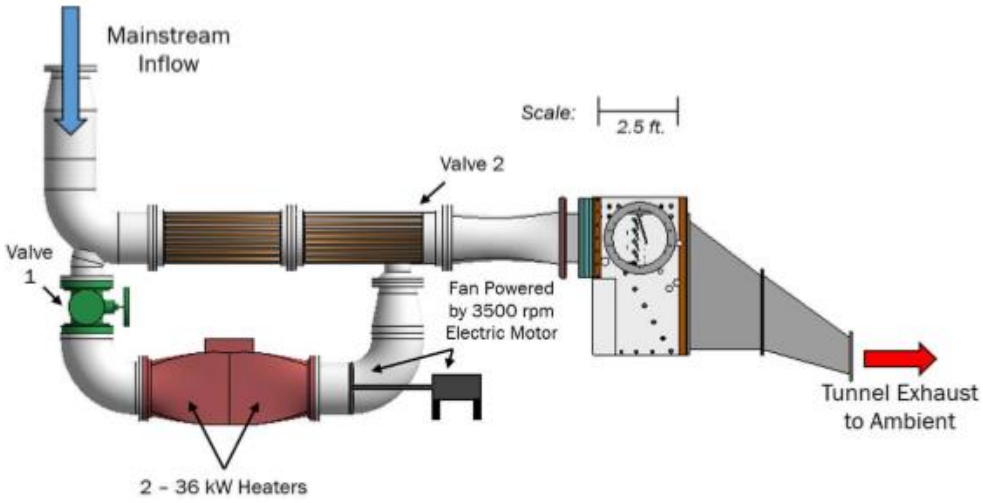

Figure 2. Virginia Tech Transonic Wind Tunnel

Once the pneumatically controlled valves are opened, supplied air then travels through a parallel copper tube heat exchanger prior to the turbulence grid that imparts the desired temperature in the mainstream flow. For heat transfer experiments, the copper tubes are heated by two 36 kW heaters in a closed loop forced-convection circulation process driven by a motor-fan system prior to blowdown. During the heating process, valve 1 is opened while valve 2 remains closed to prevent pre-heating to the test section. Temperature measurements are observed using K-type thermocouples at the heater as well as T-type thermocouples mounted on the heat exchanger tubing to ensure repeatability of mainstream flow conditions. Once the heat exchanger tubing reaches the desired temperature, the valve positions are reversed prior to the initial blowdown control sequence. The tunnel's test section is modular in design and has been utilized for testing of various cascades and assorted turbomachinery components in previous studies. Further descriptions and testing methods can be found in Mayo et al. [20], Roy et al. [12], Nasir et al. [21], and Holmberg and Diller [22], including more not listed.

B. Test section and Linear Cascade

This study investigates a linear cascade of a 1st stage NGV consisting of 4-equally spaced vane profiles. Figure 3 provides the internal layout of the associated assembled test section, and Table 1 lists the geometric details of the cascade. Upstream of the test section lies the turbulence grid intended to impart a freestream turbulence (Tu) of 16% intensity matching engine-like conditions of NGV inlet flow. Nix et al [23] more thoroughly describes the application and validation of the passive turbulence grid. Other related operating conditions are listed in Table 2. Inside the test section, half-profile vanes at the top and bottom of the cascade insert along with a mounted tailboard downstream of the top two vane passages improve flow periodicity during blowdown.

Table 1. Mainstream flow condition

Inlet Mach number, Ma_{Inlet}	0.10
Outlet Mach number, Ma_{Exit}	0.85
Exit Reynolds number, Re_{Exit}	1.5×10^6
Inlet turbulance intensity, Tu	16%

Table 2. Details of 1st stage NGV linear cascade

Axial chord, C_{ax}	50 mm
True chord/axial chord, C/C_{ax}	1.82
Pitch/axial chord, P/C_{ax}	1.66
Vane inlet angle - β_1	0°
Vane outlet angle - β_2	73.5°

A total temperature thermocouple probe is mounted within the test section 4.6 C_{ax} upstream of the cascade leading edge (LE), as well as a pitot-static probe mounted 2.8 C_{ax} upstream of the LE. Twelve static pressure ports are located on the cascade endwall: 6 ports 1.4 C_{ax} upstream of the vane LE, and 6 ports 1.4 C_{ax} downstream of the vane trailing edge (TE). Pressure measurements are obtained using a NetScanner Model 98RK Pressure Scanner recording at 10 Hz. Temperature measurements are acquired through a National Instruments Compact Data Acquisition System recording at 30 Hz. These measurements assist in characterizing mainstream inlet/outlet flow conditions for analysis.

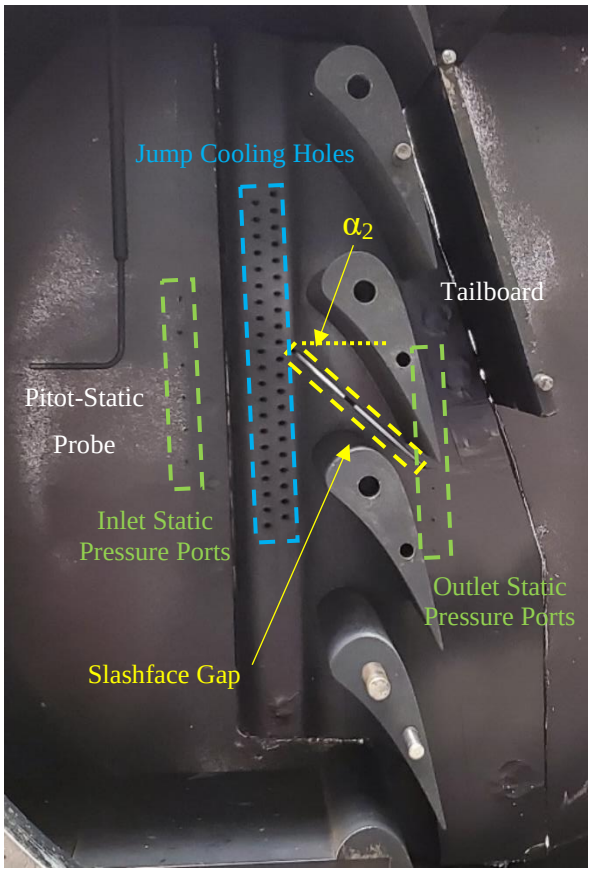

Figure 3. Test section cascade w/ NGV and endwall geometry

The endwall profile of the test section consists of an engine representative axisymmetric converging endwall under nominal operating conditions. Figure 4 details a pitchwise view of the endwall geometry. A commonly found gap at the interface of the combustor liner and vane interface is located at 0.9 C_{ax} upstream of the vane LE. A doublet staggered jump cooling arrangement is located at 0.38 C_{ax} upstream of the vane LE and centered pitchwise to the passage of interest. A slashface (SF) gap is included only in the passage of interest, starting at 0.16 C_{ax} upstream of the vane LE and ending at 0.18 C_{ax} from the vane TE, and angled 40° relative to the axial direction. The SF gap is separated into two individual cavities at 0.38 C_{ax} downstream of the vane TE in the passage. Inside the SF houses two individual stainless-steel seal strips with a relatively small thickness of 0.005” to model a more wearied condition. Further details of coolant supply interfaces are displayed in Table 3.

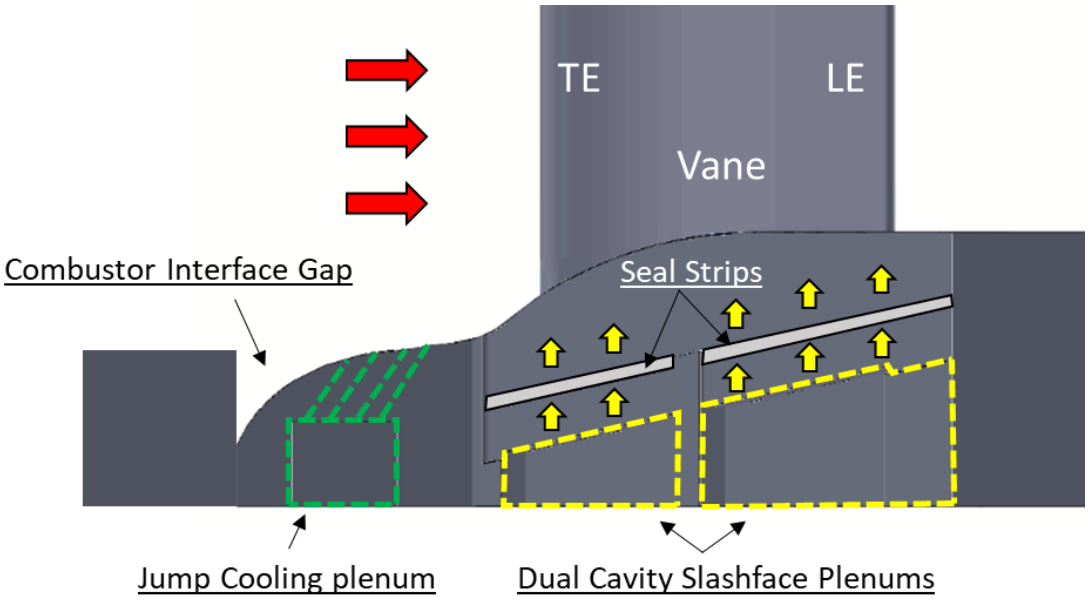

Figure 4. Pitchwise view of cascade endwall profile with coolant interface geometry

Table 3. Details of coolant interface geometry

JC Injection angle, α_1	50° from horizontal
JC Hole P/D	3.5
JC Hole L/D	1st Row - 5.3, 2nd Row - 6.0
SF gap angle, α_2	43° from axial
SF width, W_{SF}	1.87 mm
SF length/axial chord, L_{SF}/C_{ax}	1.82
SF Fwd gap length/SF length, L_{Fwd}/L_{SF}	0.40

Vane and endwall geometry of the cascade is manufactured by a Stratasys Fortus 250mc 3D printer using ABSPlus-P430 (acrylonitrile butadiene styrene) as the material. Due to printing size limitations, the vanes and endwall are printed into two separate pieces where further refinement is necessary before assembly. Each piece is sanded using various grid count sandpaper until a final acetone smoothing technique is applied to minimize manufacturing induced surface roughness and the resulting flow disturbances during testing. The jump cooling holes require additional machining as well to ensure hole diameter accuracy and smoothness. Each hole is bored through, and a nylon tube is inserted and adhered to ensure consistency in matching geometric parameters. Seal strips are then inserted between slots found along each

individual endwall mating interface when the pieces are assembled, akin to the seal strip assembly shown in Figure 1. Both test piece interfaces are then welded and sealed together with epoxy, and the resulting seam is sanded to maintain a smooth endwall. Once cured, an ultra-flat black paint boasting an emissivity of 0.97 for a spectral wavelength of 5 μm is applied to the final test piece.

C. Coolant Flow Parameters Relevance and Control

As the primary focus of this investigation is on the effects of SF leakage rates, the most critical flow parameter of supplied coolant is the mass flow ratio (MFR). However, control of the total MFR requires control of the density ratio (DR) and velocity ratio (VR) individually to meet desired coolant parameters. This coupled relationship can be seen in Equations 1-3.

$$DR = \frac{\rho_c}{\rho_\infty}$$

Equation 1. Density ratio

$$VR = \frac{V_c}{V_\infty}$$

Equation 2. Velocity ratio

$$MFR = \frac{\rho_c V_c A_c}{\rho_\infty V_\infty A_\infty}$$

Equation 3. Mass flow ratio

Sibold [19] previously investigated the effects of DR on purge jet cooling and found this parameter to be critical in accurately assessing film cooling performance in endwall heat transfer studies. A DR of 1.95 is employed for all test conditions to best represent engine-like leakage conditions. This is achieved by utilizing a controlled mix of compressed air and Sulfur Hexafluoride (SF_6). Teekaram et al. [24] pioneered this technique and demonstrated the validity of using foreign gas mixtures to simulate high density coolant. As the DR remains fixed for all test cases, variation of the VR is the key parameter to alter for each test case. However, the

upstream jump cooling parameters remains consistent to isolate the effects of varying SF MFR. Therefore, only the VR is varied for the SF leakage throughout the study.

Achieving the desired cooling parameters requires special attention to the diversion of coolant supply to each of the 3 individual plenums. The coolant is supplied from a 100-gallon buffer tank filled with compressed air at 120 psi and a Size 200 specialty gas cylinder containing industrial grade SF_6. Two independent plumbing branches regulate both compressed air and SF_6 supplies individually enabling control of overall coolant mass flux and density. The mass flow through each line is simultaneously calculated using a Lambda Square beveled and corner-tapped orifice plate, a T-type thermocouple, and static pressure ports upstream and downstream of the orifice in compliance with ISO 5167: Part 2.

Following the mixing of the gases by convergence of the two branches, the supply line then branches into three individual lines intended to supply each individual coolant plenum. The volumetric flow rate is respectively recorded for the two lines supplying coolant to both Slashface plenums using a rotameter and camera. Needle valves located upstream of the rotameters are installed inline to allow precise control over coolant flow rate. Between the needle valve and rotameter include ports to measure both static pressure and temperature to derive individual mass flow rates. Solenoid valves are employed to prevent coolant flow into the test section prior to blowdown that would otherwise alter endwall surface temperature prior to introducing mainstream flow. Temperature and pressure measurements at the plenum based the derivation for DR calculations.

D. IR Thermography

A FLIR A325sc camera with a spectral range of 7-13 μm is used to measure the endwall temperature of each pixel at a sampling rate of 30 Hz. Between the IR camera and the cascade within the test section lies a rectangular Germanium (Ge) optical window with a broad band anti-reflective (BBAR) coating offering an average optical transmission of 95% of the spectral range of interest. Figure 5 displays the measurable area of the cascade endwall passage of interest through the Ge window opto-mechanical assembly. The camera is calibrated to account for systematic errors resulting from the window's spectral absorption and reflection, slight endwall curvature, and imperfect black body from the painted endwall. This calibration uses a thermocouple mounted on the mid-passage endwall surface to simultaneously record endwall

temperature along with the camera during endwall heating within the temperature range of interest.

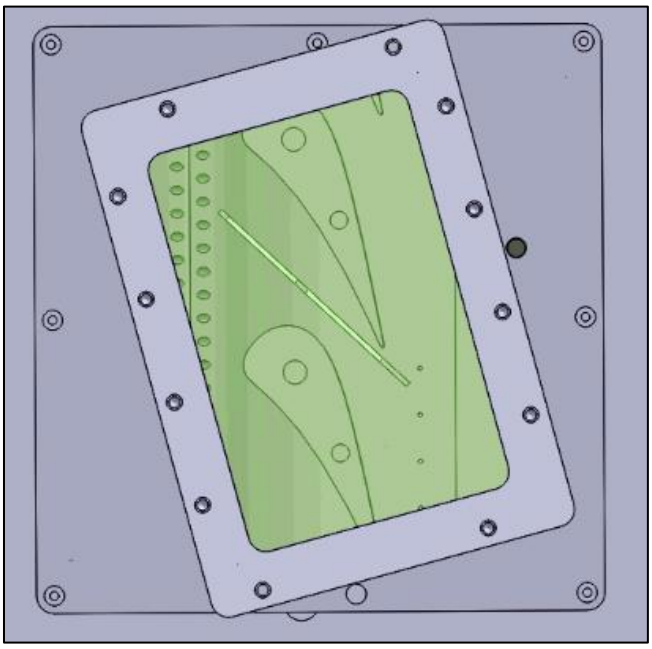

Figure 5. CAD model of opto-mechanical assembly from the IR camera view

E. Data Post-processing approach

As the IR camera obtains endwall temperature at each pixel location over the duration of the experiment, the heat flux (q") can be calculated as a function of time using a technique developed by Cook and Felderman [25]. The practicality of this expression lies in the assumption of a one-dimensional semi-infinite conduction model to apply a numerical expression shown in Equation 4 and eliminate the need for integration that is typically difficult when evaluating the upper bound.

$$q_n^{"}(t_m) = \frac{2(\sqrt{kC_p\rho})_0}{\sqrt{\pi}} \sum_{i=1}^{m} \frac{T(0,t_i) - T(0,t_{i-1})}{\sqrt{t_m - t_i} - \sqrt{t_m - t_{i-1}}}$$

Equation 4. Cook Felderman numerical heat transfer expression

Another assumption to account for is that the thermal properties of the medium do not considerably change within the frame of analysis. These assumptions are applicable in this study due to the low thermal conductivity of the cascade material, ABSPlus-P430 ($0.150 < k < 0.200$ W/m-K), a short blowdown window of no more than 9 seconds, and the relatively large thickness of the endwall throughout the passage. Like most numerical analyses, the accuracy of this technique is dependent on the temporal resolution. An endwall temperature sampling rate of 30 Hz ensures the resolution is sufficiently fine to confidently employ the expression above.

Additional key convective heat transfer parameters are reduced using the Dual Linear Regression Technique (DLRT) outlined in Xue et al. [26]. This technique is especially useful in transonic applications by accounting for compressibility effects in recovery temperature prevalent in high speed mainstream conditions. Another additional benefit is the ability to take heat transfer measurements during a transient tunnel blowdown rather than a steady state blowdown. Using the governing expression, Equation 7, both heat transfer coefficient (HTC) and adiabatic film cooling effectiveness (η) are simultaneously calculated using the most appropriate local recovery temperature (T_r). The DLRT applies a linearized combination of the definition of HTC for a film cooled surface and η in the effort to address the "Three Temperature Problem" and iterate to the most appropriate T_r using regression analysis.

$$\eta = \frac{T_r - T_{aw}}{T_r - T_c}$$

Equation 5. Adiabatic film cooling effectiveness for high speed turbine application

$$HTC = \frac{q''}{T_{aw} - T_w}$$

Equation 6. Heat transfer coefficient for the endwall surface

$$\underbrace{\frac{q''}{T_r - T_c}}_{y} = \underbrace{HTC}_{m}\underbrace{\frac{T_r - T_w}{T_r - T_c}}_{x} + \underbrace{\eta HTC}_{b}$$

Equation 7. Linearized DLRT governing equation

These convective heat transfer parameters are highly dependent on local endwall flow field factors. To ensure the validity of the DLRT, the window of selected data is slightly delayed post initial blowdown allowing flow to develop and minimize transient aerodynamic conditions. An example of the selection window is shown in Figure 6a. Following the definition of the recovery temperature,

$$T_r = T_\infty \left(\frac{1 + r\frac{\gamma - 1}{2} Ma^2}{1 + \frac{\gamma - 1}{2} Ma^2} \right) = T_\infty C_r$$

Equation 8. Recovery temperature simplified using recovery coefficient

T_r is estimated by determining the recovery coefficient (C_r) which minimizes regression uncertainty. This technique has adopted a two-test regression strategy, one with ambient coolant and another with chilled coolant. Consistent mainstream conditions between coupled tests maintains similar endwall flow profiles and related heat transfer parameters but varying the coolant temperature disperses the data to minimize the variance.

Figure 6 shows the resulting DLRT strategy on a single pixel throughout the experiment duration. Figures 6(a) and 6(b) display the resulting temperature measurements with the temporal window used to apply the DLRT. This study further improves the DLRT by creating unique temporal windows for each test run to account for differences in mainstream conditions. The data markers in Figure 6(c) are the result of calculating the x and y portions of Equation 7 modeled in the linear regression analysis. Estimating the true T_r comprised of an iterative process of evaluating the coefficient of determination (R^2) from the regression analysis throughout both experiment durations for a range of typical C_r values. HTC and η are found using the linear relationship from Equation 7 and concluded using the C_r which corresponds to an R^2 value that is

closest to unity. This process is repeated for every pixel measured by the IR camera, and a set of heat transfer parameters is gathered for each spatial location.

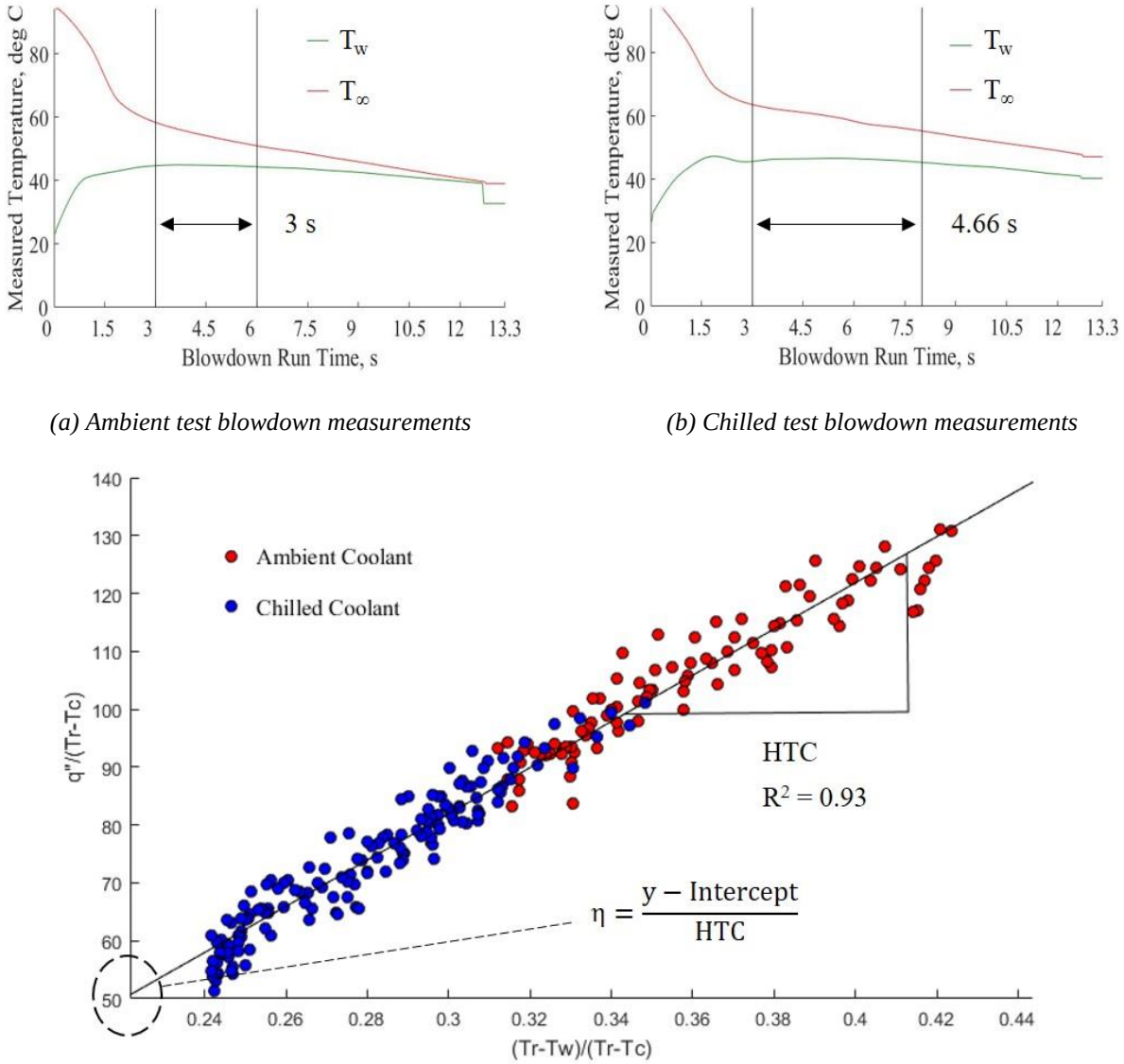

(a) Ambient test blowdown measurements

(b) Chilled test blowdown measurements

(c) DLRT applied to both chilled and ambient test's temperature measurements

Figure 6. Example of DLRT applied on a single pixel

Although the heat transfer parameters provide adequate indicators of thermal performance in turbine endwall film cooling, the relationship between η and HTC can sometimes be directly correlated depending on local endwall flow profile characteristics despite the presence of film cooling. The introduction of fluid from the coolant injection interfaces can

disrupt near endwall flow and impart additional turbulence within the boundary layer. Consequently, the local HTC may increase past the insulating benefits provided from the presence of coolant and the resulting net heat flux to the endwall increases when injecting coolant. The gas turbine heat transfer and film cooling research community has attempted to account for this adverse effect in HTC during analysis by assessing the Net Heat Flux Reduction (NHFR). The NHFR evaluates the reduction of endwall heat flux that coolant injection provides using local HTC found from both cooled and uncooled geometry. This allows for the valuation of film cooling to account for variations in HTC and η under a single term.

$$NHFR = \frac{q''_{w,uncooled} - q''_{w,cooled}}{q''_{w,uncooled}} = 1 - \frac{HTC_{cooled}}{HTC_{uncooled}}\left(1 - \frac{\eta}{\varphi}\right)$$

Equation 9. Net Heat Flux Reduction in applicable expression

More information on NHFR is provided in Li et al. [27] and Sen et al. [28]. Integrating HTC and η into the definition of NHFR provides an applicable expression that introduces overall film cooling effectiveness (φ).

$$\varphi = \frac{T_r - T_w}{T_r - T_c}$$

Equation 10. Overall film cooling effectiveness definition

Mick and Mayle [29] found that the average φ is around 0.6 for typical gas turbine engines assuming realistic turbine inlet temperature, coolant temperature, and endwall temperature. This value is used for all NHFR calculations throughout this study.

Uncertainties for the resulting convective heat transfer parameters were previously evaluated following the Moffat's perturbation method [30] that expands on the method outlined in Kline and McClintock [31]. HTC and η expressions are further expanded to include the pertinent measured variables used in the reduction: endwall surface temperature, mainstream temperature, and coolant temperature. The endwall surface temperature uncertainty follows the FLIR A325sc camera's reported temperature measurement uncertainty of ± 2.0 °C, or ± 2.0% if

greater. Both the mainstream temperature and coolant temperature are measured with standard T-type thermocouples. ASTM E230 provides the standard limit of error for T-type thermocouples as ± 1.0 °C, or ± 0.75% if greater.

Previous evaluation for the experimental uncertainty in the relating heat transfer parameters were performed by Sibold [19] and found to be a maximum of ± 9.6% of HTC and ± 0.1 of η. The near identical experimental setup regarding operating conditions, cascade geometry, and measurement instrumentation between Sibold [19] and this investigation retains the applicability of the previous uncertainty analysis. One important aspect to consider is that the uncertainty is only applicable on the regions of the endwall where the one-dimensional semi-infinite conduction model is valid.

Results and Discussion

A. Preamble

The subsequent discussion will include the following in order: CFD validation, passage aerodynamics, experimental heat transfer performance results, and a computational fluid dynamics (CFD) simulation comparing dual against single cavity configurations. The dual cavity configuration creates a complicated flow field structure and is useful in understanding prior to examining heat transfer results. Both experimental flow visualization and CFD analysis are supplementary in understanding the flow patterns, so the CFD is validated first. Experimental results will cover four test case conditions outlined in Table 4 with the baseline case highlighted. Comparisons of HTC, η, and NHFR will highlight the deviation of key convective heat transfer parameters each case presents. A CFD simulation is carried out to investigate the differences of using a single, rather than a dual, slashface cavity on the same cascade geometry. The simulation results are compared with experimental findings to ensure the validity before further analysis.

Table 4. Experimental test matrix w/ baseline case highlighted

Case	JC Purge MFR	SF Fwd MFR	SF Aft MFR
1	1.85%	0.32%	0.32%
2	1.85%	0.16%	0.48%
3	1.85%	0%	0.48%
4	1.85%	0.16%	0.16%

B. CFD Validation

Although current published literature has broadly investigated the use of coolant supply in the slashface gap, the use of dual cavities supplied by individual cavities has yet to be studied. As Roy et al. [12] states, the endwall coolant distribution is highly dependent on the relative gap location and cascade design. This facet of endwall film cooling coupled with the slashface gap prevents any direct comparison of the results found in this study to previous single cavity slashface studies to isolate and evaluate the effects of the novel dual cavity geometry. A computation fluid dynamics simulation is employed on the pertinent cascade geometry to analyze differences in endwall flow profile and film cooling performance between the use of a single slashface cavity and dual slashface cavities. These results are valuable in understanding the aerodynamic behavior and changes of gas ingestion and egression along the slashface gap.

The numerical simulations in this study are carried out by solving the 3D steady-state Reynolds-averaged Navier-Stokes equations using ANSYS Fluent v19.2. The working fluid consists of ideal air whose specific heat, thermal conductivity, and viscosity are estimated using kinetic theory. The Reynolds Stress turbulence model with low-Re correlations and compressibility effects options are used for the following simulations to better predict the endwall thermal performance in high speed flow. Shear flow corrections and viscous heating are also taken into consideration.

A pressure-velocity coupled algorithm is adopted with second-order upwind momentum and energy equations. The calculations were considered to be converged when the root mean square residuals of the continuity, momentum, energy and turbulence kinetic energy equations reached 10^{-5} and the mass flow rate of the inlet did not change more than 0.01% for 50 iterations. The computational domain and mesh in this study are presented in Figure 7. A multi-block structured mesh is generated with ICEM CFD. The mesh near the solid surfaces is further refined to $y^{+}<1$, driving the total grid number to 7 million, to meet the requirement of the turbulence model used. Translational, periodic boundary conditions are imposed along the pitchwise direction. Table 5 details the grid independence results resulting in the use of a 10.81 million grid count.

Table 5. Grid independence test results

Grid number (10^6)	Averaged T_w (K)
5.78	335.8
8	336.64
10.81	336.83
13.44	336.87

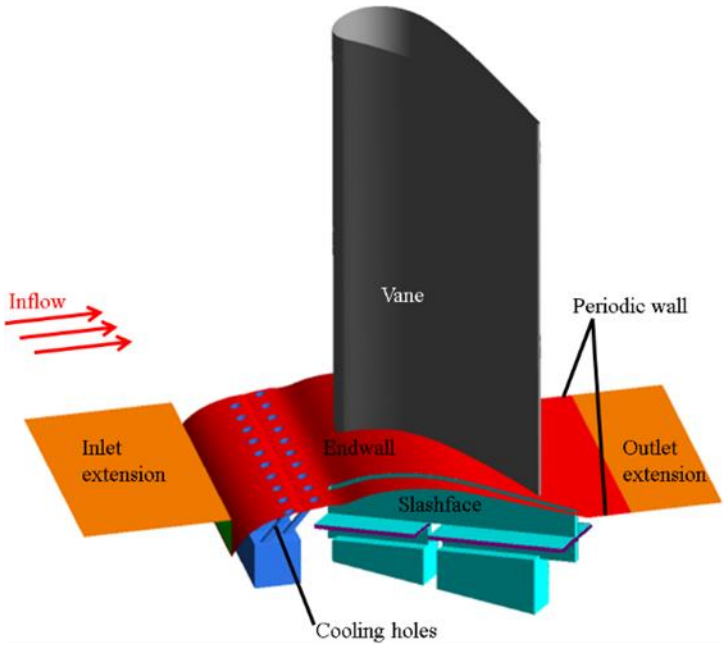

(a) Geometric model

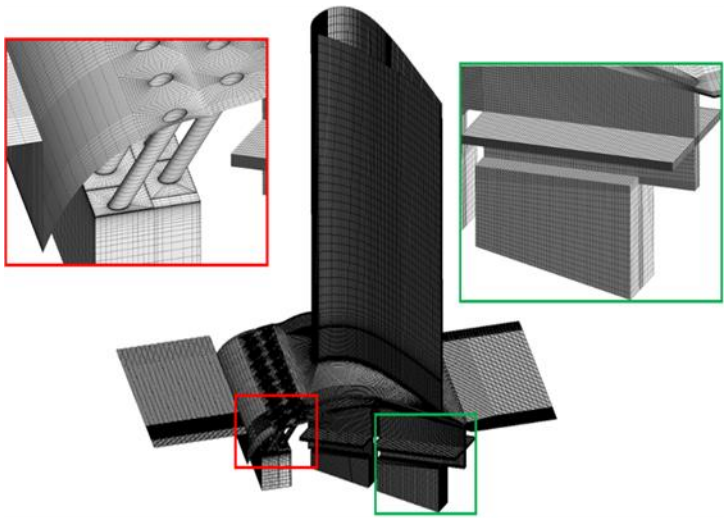

(b) Mesh

Figure 7. Computational model and mesh

Because the boundary layer of the approaching mainstream flow at the endwall can significantly impact the working fluid's thermal performance, the incoming pressure and temperature are defined using measurements from identical experimental tests. To further match the observed experimental conditions, an inlet freestream turbulence intensity of 16% and outlet pressure of 1 atm is implemented in the simulation as well. The coolant temperature (T_c = 298 K) for all three plenums remains constant throughout the simulation.

A two-simulation technique is used to measure the endwall heat transfer. The endwall temperature (T_w = 300 K), which remained constant across simulations, is applied to determine the resulting adiabatic endwall temperature and the heat flux separately. The HTC and η are then calculated using Equation 6 and Equation 11, respectively. A caveat in applying Equation 11 for the numerical solution is that it does not consider compressibility affects by accounting for losses within the recovery temperature. Accurately employing the recovery temperature requires resources outside of the present study's scope and can be further improved upon in future work.

$$\eta = \frac{T_\infty - T_{aw}}{T_\infty - T_c}$$

Equation 11. Adiabatic film cooling effectiveness used in CFD

Prior to reviewing the simulation results, the computations pertaining to the dual cavity configuration are compared with experimental results to ensure the validity of the simulation. The experimental flow visualization is shown in Figure 8 with limiting streamlines found from CFD superimposed onto the endwall oil paint. There appears to be a high agreement with the experimental flow visualization, as the computed streamlines match closely with the oil paint streamlines in both the flow direction and curvature behavior. Specifically, the green and blue oil streaks along region A below the slashface gap match closely in terms of the streamline path. Above the gap towards the PS, region B, shows agreement with the flow visualization in two ways: First, the streamlines show a relatively large distance from the vane wall and matches the contour of the oil paint. Second, there appears to be separation of the flow near the gap due to ingestion that will be further discussed. Region C contains both the high velocity egression flow path and the PV crossing the gap in which both the simulated streamlines and the flow

visualization distinctly match. Above C lies a stagnation point near where the yellow paint accumulates that is discussed further in the flow visualization

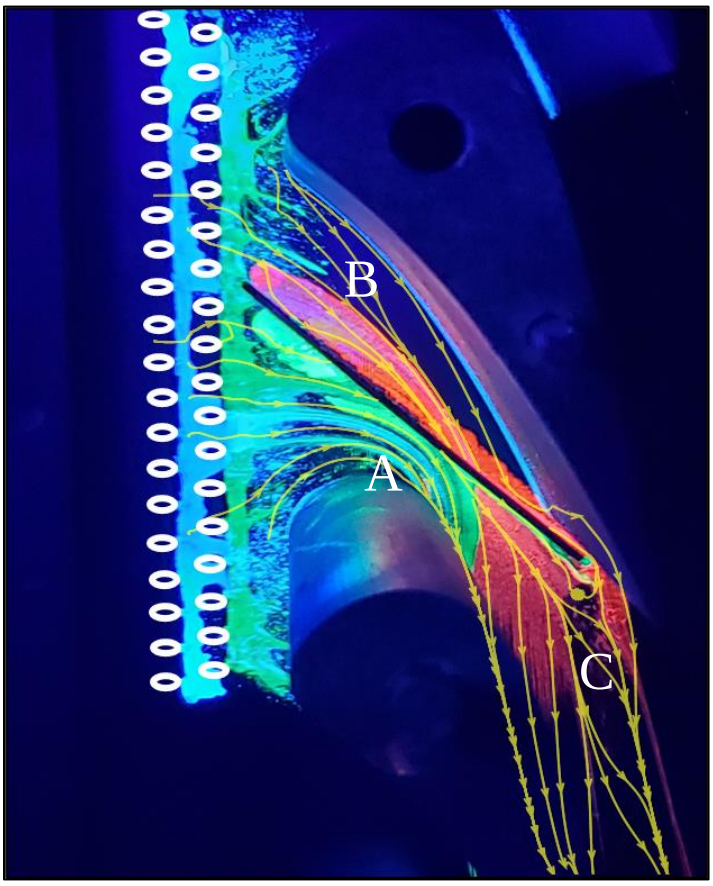

Figure 8. CFD limiting streamlines superimposed on experimental flow visualization

Figure 9 compares both numerical and experimental passage endwall HTC and η distributions. In general, the numerical coolant coverage condition is overpredicted in magnitude, as compressibility effects are not accounted for in the recovery temperature. However, the distribution maintains similar patterns of coolant coverage also found experimentally. The primary high and low heat transfer regions can be observed on the same locations on the endwall, although the overall predicted HTC is lower in the simulation results. This disagreement can originate from the inaccuracies of CFD modeling turbulent behavior that typically increases heat transfer levels.

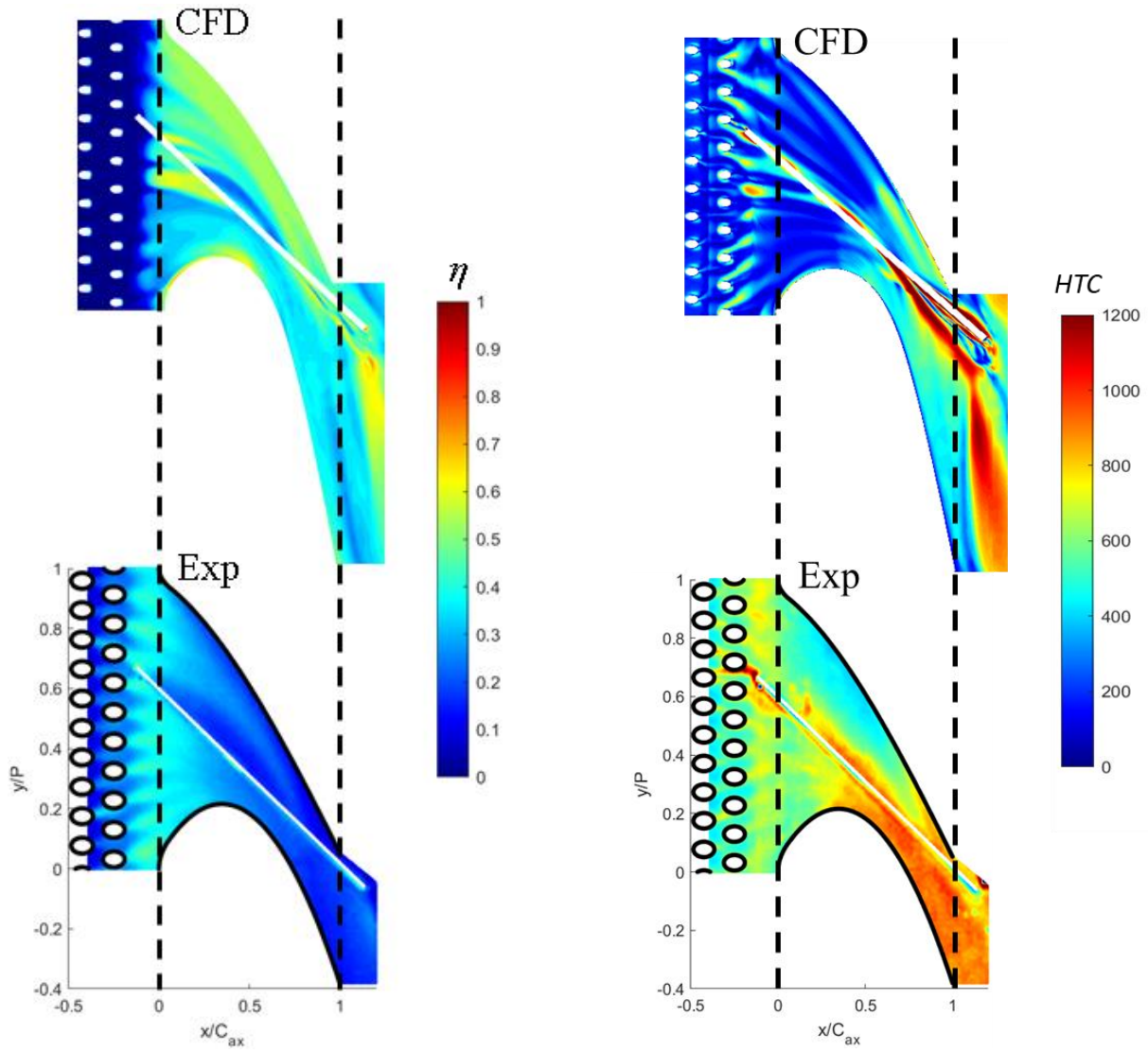

Figure 9. CFD comparison of η and HTC distributions with baseline experimental results

Critical patterns of the adiabatic effectiveness distribution suggest agreement with particular coolant flow interactions. For example, the coolant from the upstream staggered holes penetrate the pressure side endwall throughout the passage. However, a crescent shaped region along the slashface gap interface, starting around 0.2 C_{ax} until the passage flow meets the gap, possesses nearly no coolant coverage. Another distinguishable pattern is the increase in η following the reattachment of the egressed gas from the slashface gap. The CFD results show no increase in η immediately following the gap, but an increase at a distance along the egression flow path indicating the egression behavior is adequately modeled.

Despite the simulation's limitation in underpredicting the endwall turbulence's effect on heat transfer, the patterns of heat transfer augmentation suggest agreement. Discrete, high heat transfer regions in the pitchwise direction can be observed downstream of the injection holes between $-0.2<x/C_{ax}<0$ from jump cooling purge jet reattachment, irrespective of CFD underpredicting the spread of heat transfer levels. On the SS endwall at mid passage near 0.4 C_{ax} lies a region of increased heat transfer throughout the remaining passage area that both CFD and experimental results share. Regions of increased HTC around the gap can also be observed with a smaller spread in the simulation results. Both results also share a smaller region of increased HTC near the pressure side vane at the trailing edge. The similarities of thermal performance results for both numerical and experimental results indicate that the simulations provide an adequate estimation of turbine passage flow interaction with the slashface geometry

B. Passage Aerodynamics

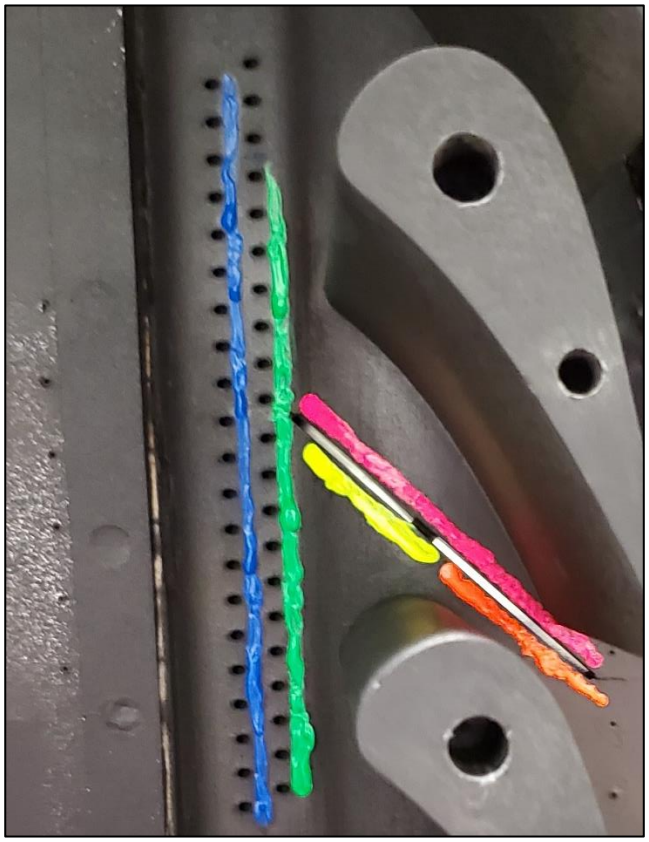

Figure 10. Flow visualization oil paint application prior to blowdown

The oil paint flow visualization technique is a qualitative tool in understanding the overall flow behavior. Fluorescent paint pigments are mixed using 100 cSt silicon oil in the various colors shown above. The green and blue paint streaks spanning the pitch are used to track coolant behavior regarding ingestion and egression as well as overall endwall coolant coverage. The pink on the PS endwall is meant to track the passage flow and resulting passage vortex (PV) behavior. Yellow and Orange paint streaks attempt to provide direction of ingestion and egression for to each cavity. This experimental run used the baseline conditions of JC purge and SF leakage MFR. Since heat transfer measurements are not necessary, the coolant is activated prior to the mainstream to prevent ingestion patterns not seen in quasi-steady state flow behavior.

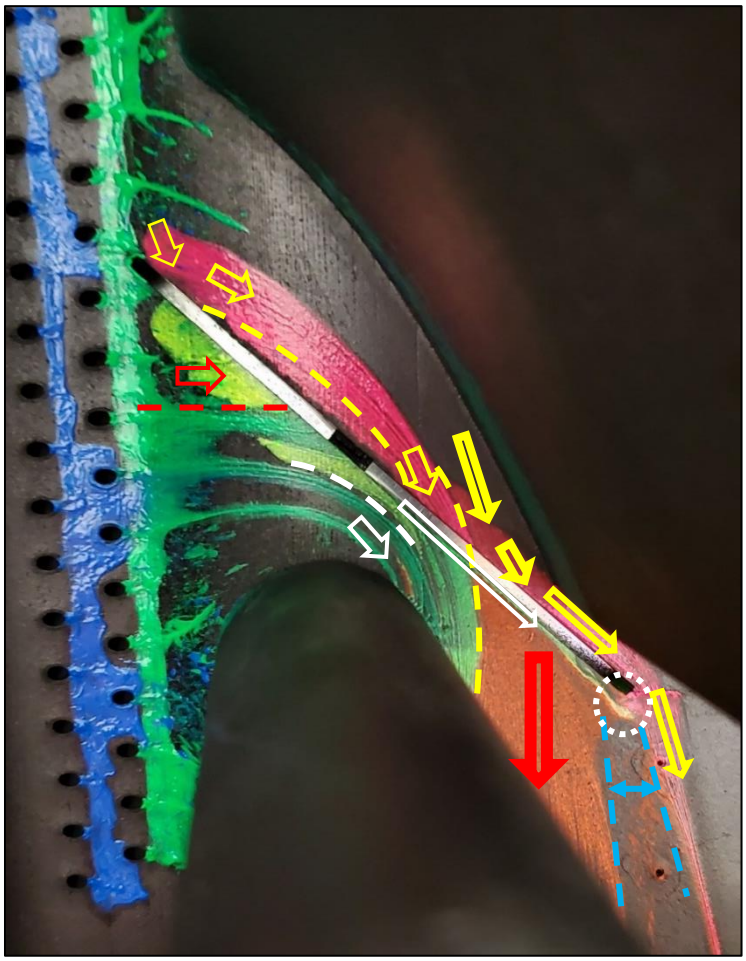

Figure 11. Entire flow visualization results for baseline case

The subsequent streak lines suggest many different flow patterns forming around the SF gap. Starting on the PS at the Fwd cavity tip in Figure 11, the pink paint close against the gap interface before the yellow dotted crescent line suggest initial ingestion and soon travels towards the PS. No ingestion is taking place on the PS along the yellow dotted crescent until the PV attempts to cross over the SF gap, but the lack of pink on the SS points to immediate ingestion into the gap. The red arrow by the Fwd cavity shows the green coolant and yellow paint traveling straight into the SF gap and does not reach the PS.

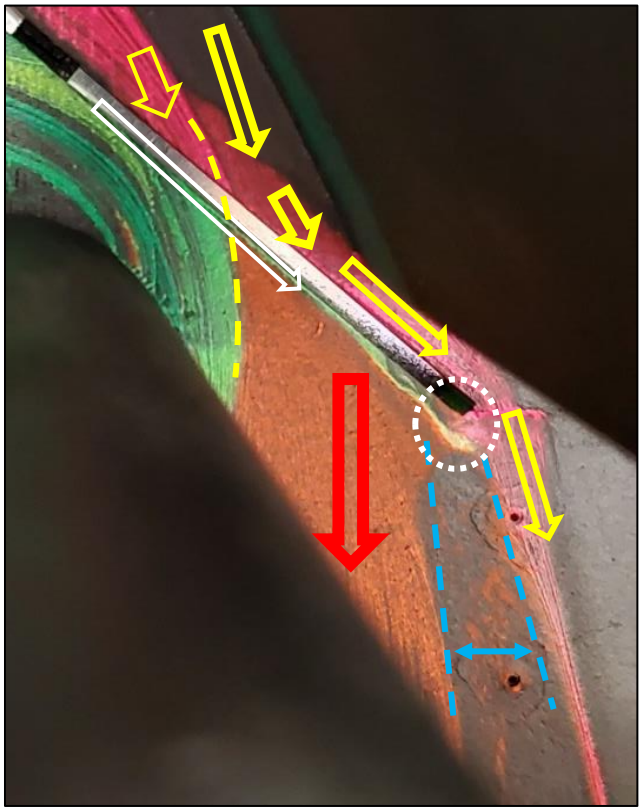

Figure 12. Aft portion of flow visualization

Endwall pressure is typically at the lowest in the passage throat, and the relative difference from cascade inlet pressure until near vane TE pressure is magnified due to high speed transonic mainstream conditions. Ingested gas inside the Aft cavity compresses at the tip and forms a large pressure differential with the relatively low mainstream endwall pressure causing high spanwise velocity to egress from the gap. The orange paint represents the high spanwise velocity path along the SS endwall of the Aft cavity. Above is a slim line of green paint along the

SF gap that covers the region of the endwall that the egressed flow separates from during ejection. The pattern of this green paint appears to grow larger as the geometry continues downstream. This can be attributed to increases in ejection momentum from the declining mainstream static pressure causing larger areas of separated flow before endwall reattachment. Another key interaction within this particular flow is a complete blockage of the PS endwall flow from crossing the gap at that location. Instead, the downstream passage flow either ingests directly in the gap or presses between the TE and SF gap as it travels past the end of the SF tip until interaction with periodic flow from another passage.

A region with high endwall pressure is outlined between the blue dotted lines where the two flow paths of the orange and pink paint are prevented from penetrating. This region is where the newly formed vortex, referred to as the egression vortex in this study, forms after flow originating from the tail-end of the Aft cavity ejects at a high spanwise velocity and reattaches to the endwall. This process is further discussed in detail by Lynch and Thole [9]. Green paint is collected at the tail-end of the Aft cavity, suggesting that upstream ingested coolant stagnates inside the cavity before ejecting out. Ingested flow in the Fwd cavity can reach the Aft cavity, as the barrier separating the two does not fully each the endwall height to fully encapsulate the two cavities.

The white dotted circle above the egression vortex outlines a flow behavior not previously observed in past literature concerning SF geometry. Stagnation occurs here due to the surrounding flow profiles discussed. Upstream flow that is high in velocity tangential to the SF gap travels through the passage, under the separated, ejected flow, then stagnates at a location that is surrounded by flow that creates high pressure environments due to endwall reattachment. This newly observed phenomenon exists due to the flow environment created by the novel dual cavity geometry tested under transonic conditions.

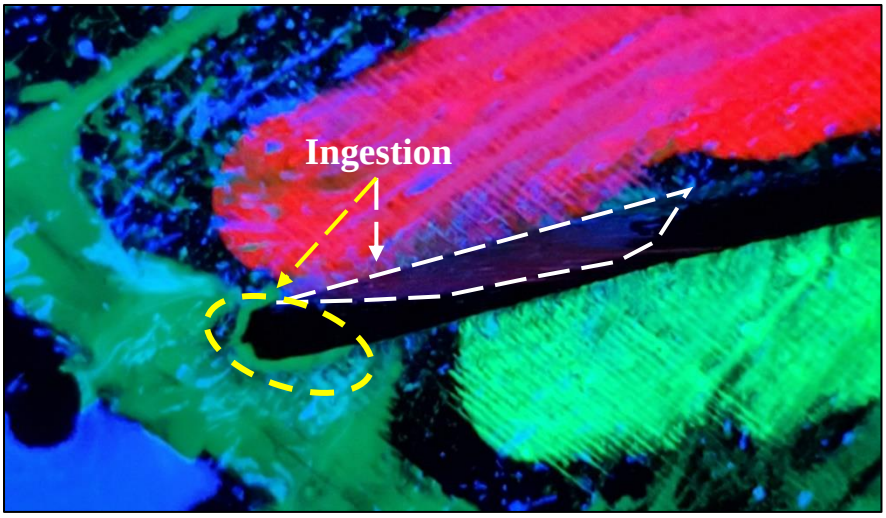

Figure 13. Flow visualization results surrounding the SF gap Fwd cavity

Ingestion is found along the Fwd cavity as green coolant paint coaxes along both sides of the tip. The blue and red paint along the wall indicate that flow from the PS endwall initially ingests hinting that the Fwd cavity extends far enough upstream to interact with the Horseshoe Vortex (HSV). This is also direct evidence of upstream coolant ingestion that supports the pattern of a reduction in coolant coverage on the PS endwall when the SF gap is introduced in previous studies [12]. Despite the ingested coolant less able to shield the endwall, a benefit to this ingestion is the HSV weakening due to the thinning of the HSV boundary layer. These effects can propagate downstream throughout the passage and can lead to a weaker pressure side leg vortex (PLV), suction side leg vortex (SLV), and PV as well as additional secondary flows to establish a more favorable cooling environment throughout the passage.

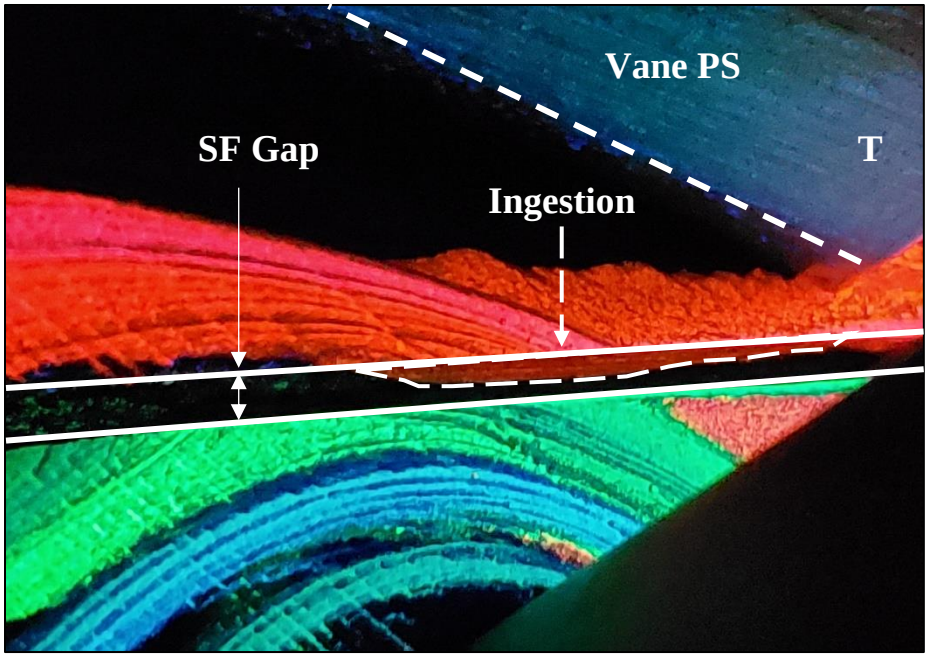

Figure 14. Flow visualization results surrounding the SF gap Aft cavity

As the PV attempts to cross over the Aft cavity gap, the endwall flow is completely ingested as evidenced in the dotted white outline. This interaction is one of the most critical behaviors regarding near throat SS endwall thermal performance. Ingestion here can either further thin the PV boundary layer, creating a less turbulent environment for film cooling retention, or it can cause separation and strengthen the secondary flow. Sibold [19] detailed how purge jet flow can reenergize the boundary layer for improved secondary flow suppression; however, a jet with enough momentum can cause lift off with high turbulence reattachment creating a net negative effect. This concept can be applied to the geometry presented in this study as well where low momentum ingestion, such as in the tip of the Fwd cavity, can suppress the PV, or high momentum ingestion can lead to strengthening of the PV as a result of boundary layer separation.

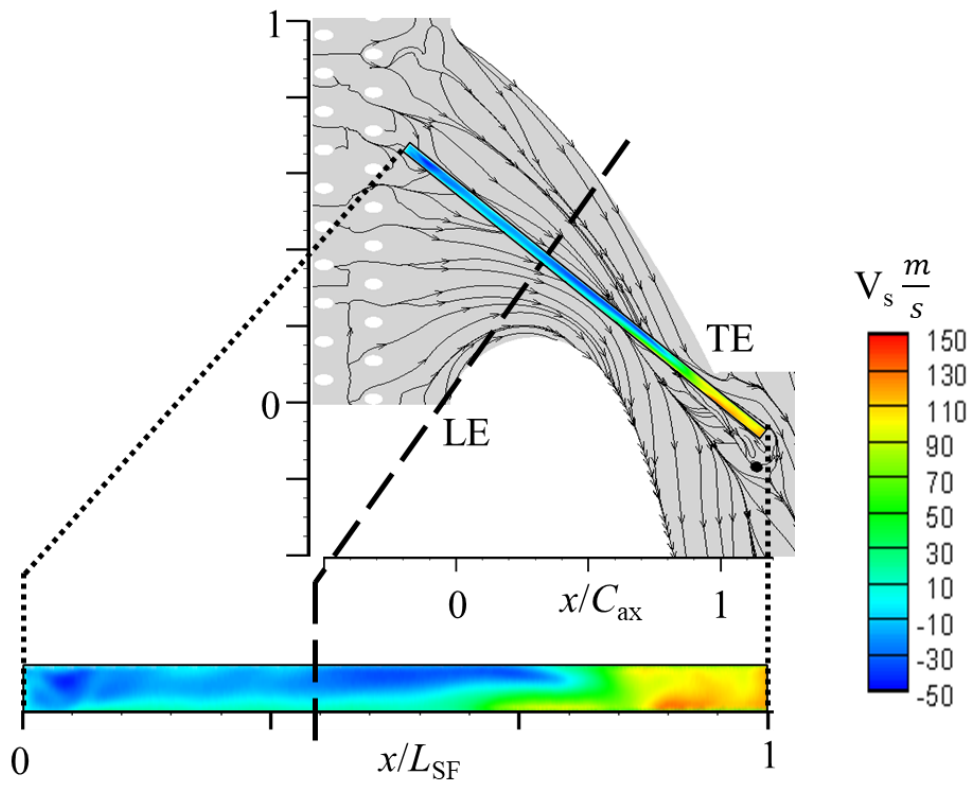

Figure 15. CFD SF gap spanwise velocity contour at baseline conditions

The computational analysis of the flow field displays the spanwise velocity distribution in the baseline case throughout the gap interface at the endwall height in Figure 15 where the cavities are separated with a dotted black line. In the Fwd cavity, the highest amount of ingestion occurs in the very beginning yet maintains a semi mass flux equilibrium throughout the remainder with small amounts of ingestion in the middle. As seen from the Figure 15 contour and Figure 11 flow viz, PS endwall flow curves away from the SF gap interface and eventually crosses close to 0.6 C_{ax} (~0.5 L_{SF}, where the Aft cavity begins at 0.4 L_{SF}). The ingestion close to the PS indicates that flow from the SS endwall crosses the net zero flow zone on the edge of the gap interface to then ingest. This could provide benefits of thinning the SLV for improved film cooling on the SS endwall. Once the PV meets the SF gap, simultaneous ingestion and egression occurs in agreement with the flow visualization. Then, flow is only ejected out of the gap with intensity increasing farther downstream and closer to SS.

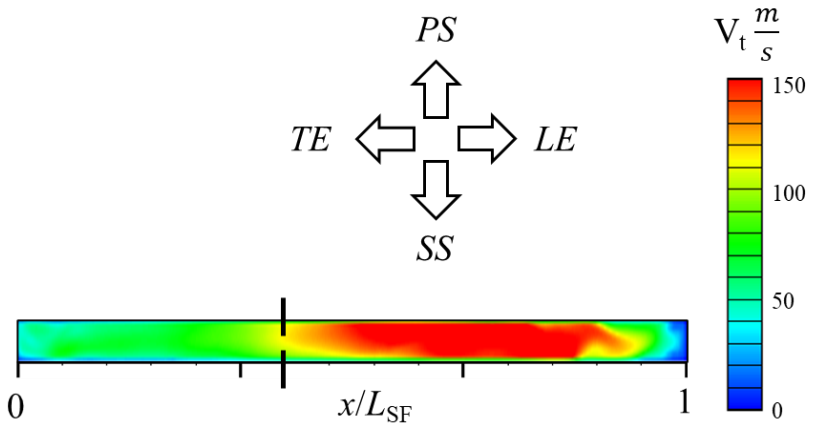

Figure 16. CFD SF gap tangential velocity contour at baseline conditions

The tangential velocity at the gap interface is descriptive in the differences between flow behavior within each cavity. Both cavities appear to have nearly uniform velocity throughout, with the Aft cavity having the most significant magnitude. The stagnation at the end along with the relatively high spanwise velocity points to a large separation that occurs from the flow originating at that point.

C. Adiabatic Film Cooling Effectiveness

The experimental results found for adiabatic film cooling effectiveness (η) are complex in interpretation, but straight forward in comparing all test cases. Just past the SF gap tip at the vane TE begins a crescent shape of nearly zero coolant coverage along the gap on the PS endwall seen on Figure 17. As indicated by Figure 13 in the flow visualization, coolant intended for coverage in the crescent shaped region is instead ingested into the gap. Unlike previous studies of slashface leakage at transonic conditions where nearly no coolant is found on the PS endwall, significant coolant coverage along the PS endwall is still achieved and retains cooling effectiveness until the PV meets the SF gap. By using two cavities, flow within the Fwd cavity stagnates and creates a more stable pressure distribution locally that alleviates drastic coolant ingestion. This ingestion also depresses the PLV and PV as significant film cooling effectiveness nearly reaches the vane wall at the TE.

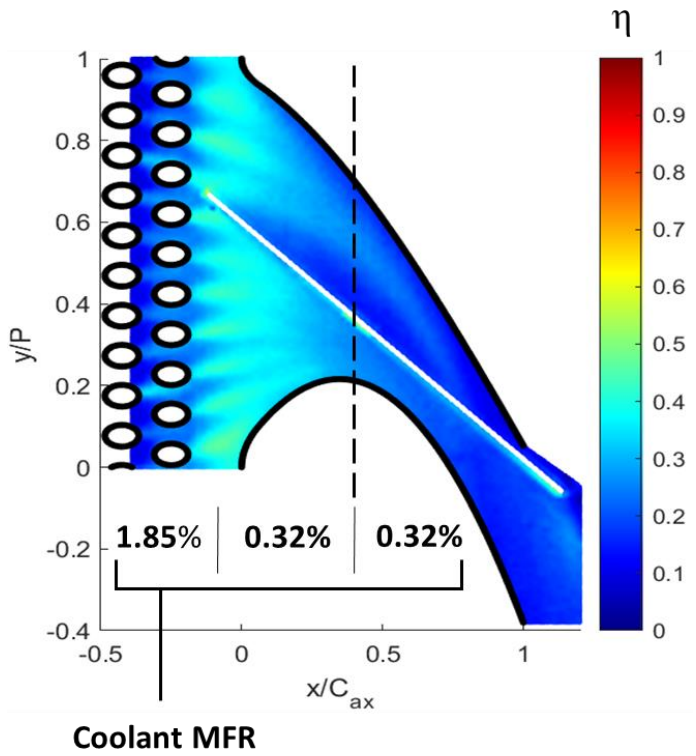

Figure 17. Adiabatic film cooling effectiveness distribution results for baseline case

The SS endwall also shows minimal film cooling retention throughout the passage contraction. The proximity to the vane wall can be attributed to a slight depression in the SLV due to upstream ingestion. The film cooling effectiveness is retained until the PV crosses over the SF gap where boundary layer separation can induce turbulent flow sweeping the endwall film cooling away. At the very end past the Aft cavity tip occupies a region with heightened film cooling effectiveness. This is credited to upstream coolant ingestion collecting at the end of the Aft cavity which then ejects and reattaches to form the egression vortex. This egression vortex carries coolant to spread upon reattachment in an inefficient manner.

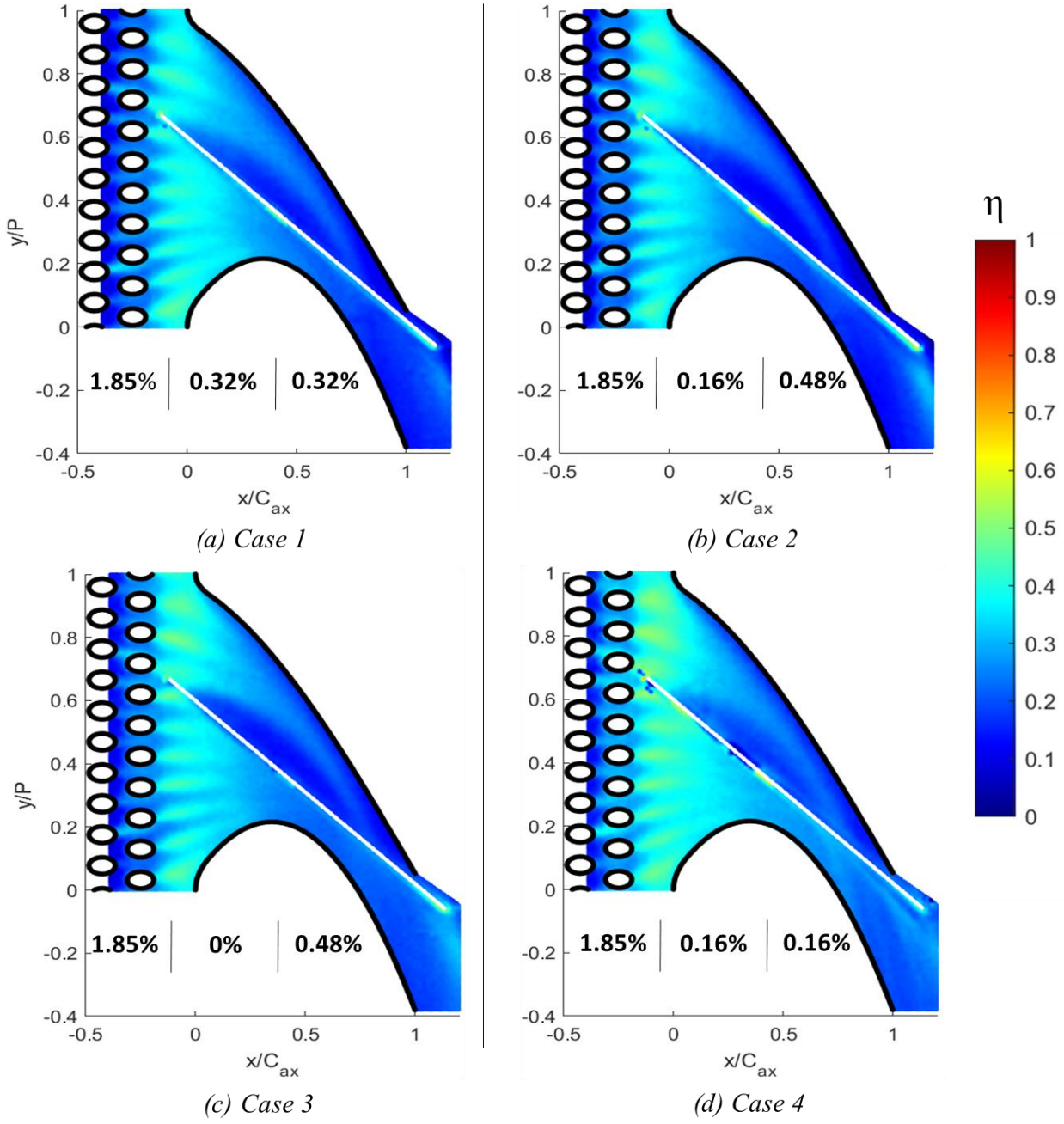

Figure 18. Adiabatic film cooling effectiveness distribution for all reported test cases

The effect that SF MFR performs in η is extremely minimal. All test cases studied have nearly negligent differences in terms of film cooling. However, there are noticeable patterns. Case 2 shows nearly identical patterns and magnitudes throughout the entire passage apart from the egression vortex. By increasing the Aft cavity MFR, η has a significant increase in this

region. This is confirmed in Case 3 where the same Aft cavity MFR bolsters a significant improvement as well.

Case 4 appears to be the only case with significant difference. The reduction in MFR created a more favorable cooling environment on the SS endwall by altering the gap interaction with the PV crossing the gap, similar to Aunapu et al. [3]. Upstream coolant traveling along the SF gap also appears to retain more cooling effectiveness traveling to the stagnation point discussed in the flow visualization, as the less intensive flow field mitigated turbulent mixing with the stream. Upstream coolant near the Fwd cavity is also able to cross over and retain more coolant coverage not observed in other cases.

Unlike previous studies where increasing MFR allows more coolant to spread on the SS endwall [13,16], reducing the total SF MFR by half increased SS endwall film cooling coverage. Understanding the exact nature of this discrepancy requires further study in this geometry. However, this behavior is most likely the direct result of the dual SF cavity causing a change in slashface gap interface pressure distribution. Any changes in ingestion and egression behavior can have substantial effects in the endwall aerodynamics throughout the entire passage. Regarding all cases, however, altering MFR does not appear to make any significant changes in endwall adiabatic film cooling effectiveness. Instead, endwall film cooling effectiveness is primarily dependent on upstream coolant. Nearly all observed differences are within the experimental uncertainty and no conclusions can be made on this heat transfer parameter alone.

D. Heat Transfer Coefficient

The heat transfer coefficient (HTC) distribution is more descriptive in flow interaction with the gap interface. Patterns of HTC are present around the Fwd cavity tip where the relative magnitude is indicative of ingestion momentum. As Piggush and Simon [11] point out, ingestion acts to thin the boundary layer of the endwall flow. This thinning assists in stabilizing the boundary layer yet increases the heat transfer as well. A large section of relatively high HTC is also present along the gap interface on the PS endwall. Instead of ingestion at the region as the cause, the lack of endwall flow in this region permits high vorticial mainstream flow to impact this area.

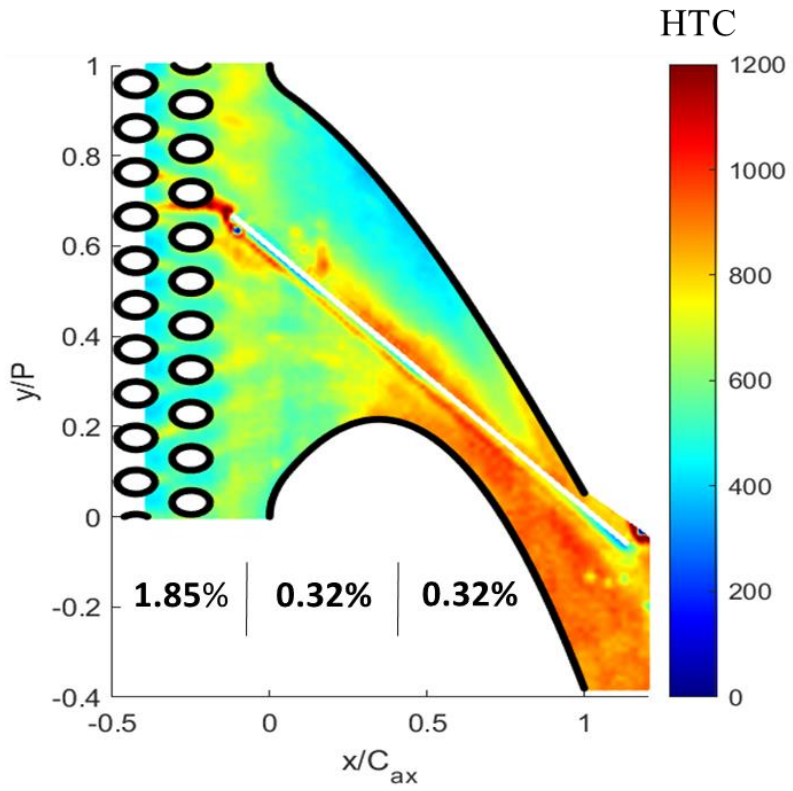

Figure 19. Heat transfer coefficient distribution results for baseline case

The heightened HTC circles just before the vane LE are a result of purge jet coolant turbulent reattachment to the endwall. As the endwall converges to flat geometry and endwall flow boundary layer no longer benefits from flow acceleration, a boarder of increased HTC appears, and high HTC remains throughout the SS endwall. As the PV crosses the gap to meet the SLV, no discernable pattern is found to indicate that the augmented vortex is active on the endwall. However, lines of heightened HTC semi tangential to the gap indicate that tangential flow along the SF gap interface has high enough tangential velocity to increase the HTC by nearly 10%. Overall HTC distribution along the SS endwall can be attributed to the reattached flow ejected from the Aft cavity. The PS of the vane TE is another region of concern as coolant is often difficult to reach this area as a corner vortex will swipe the coolant from the endwall. A particular region of low HTC can be seen at the endwall stagnation point just below the Aft cavity, although this region is too close to the SF gap inner walls to make a valid semi-infinite conduction assumption for conclusive statements.

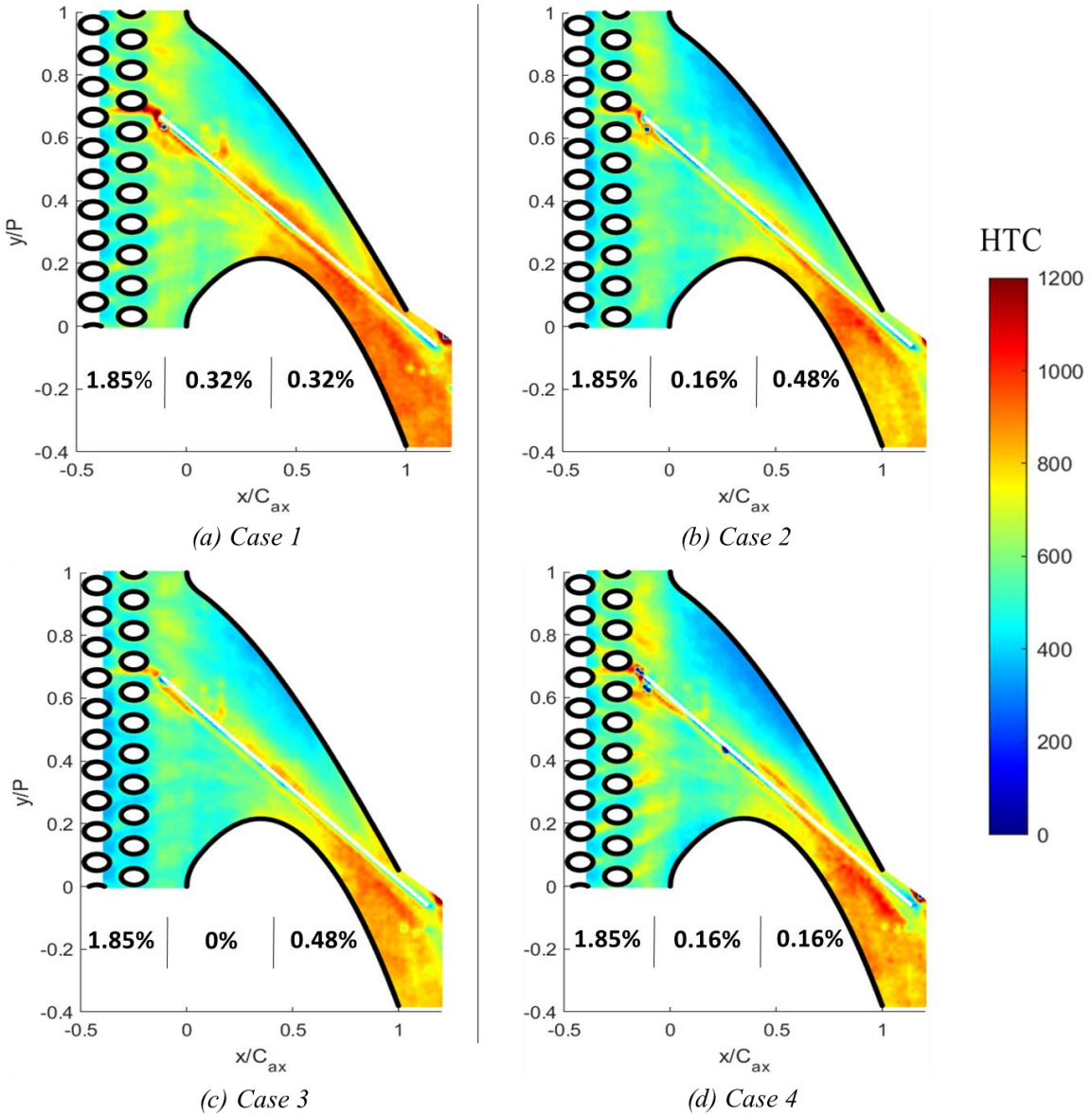

Figure 20. Heat transfer coefficient distribution for all reported test cases

Varying the SF MFR shows a much more significant difference in HTC amongst the cases than differences in η. All subsequent cases lower the Fwd cavity MFR which is reflected in the resulting relative HTC intensity. As the passage inlet Mach number is low enough to be considered incompressible (M_{inlet} = 0.1), the changes in pressure distributions that the SF MFR provides are more prevalent towards the leading edge. The heightened HTC caused by purge jet endwall reattachment is slightly mitigated across all other cases with lower Fwd cavity MFR.

This can be attributed to the change in ingestion behavior near the Fwd cavity that would cause a change in near endwall pressure gradients.

HTC patterns along the gap PS endwall and at the Fwd cavity tip are reduced with lower Fwd cavity MFR as well. An explanation for that could be the possibility of a decrease in endwall flow ingestion with decreases in Fwd cavity MFR, despite what the previous studies concluded in testing single cavity geometries at low speeds. Case 4 appeared to have performed the best on the PS endwall with low HTC on the PS vane wall interface near the TE, while Case 3 appeared to weaken either the high velocity tangential the most leading to the lowest HTC distribution along the SS endwall.

The baseline case, compared to the remaining test cases, is the outlier in terms of HTC distribution across the SS endwall near the throat. This can be attributed to the Fwd cavity MFR being higher causing changes in the tangential flow along the gap interface. Lower SF MFR typically performs better in terms of reducing HTC across the passage, especially regarding the Fwd cavity. As the differences in HTC distributions are much more apparent than η distributions, the effects behind the dual cavity SF MFR appear to be based on altering the aerodynamics of the flow within the passage. Altering SF MFR has a trivial effect on adiabatic film cooling effectiveness but has a first order effect in HTC distribution.

E. Net Heat Flux Reduction

The net heat flux reduction (NHFR) is a common analysis technique used by the gas turbine research community to consider both HTC and η into one distribution to determine the net effects. Regions closer to red, or 0, indicate that additional coolant did not provide any net reduction in heat transfer. Regions closer to blue, or unity, are completely absolved of heat transfer when coolant is introduced.

Regarding the baseline case in Figure 21, the lowest NHFR is found throughout the PS of the passage. As the dominant effect of the slashface gap behavior is ingestion and egression of coolant and hot gas, changes in SF MFR affect the flow field and related heat transfer parameters throughout the passage. Distributions of HTC also indicate that lower SF MFR provide more optimal flow patterns for improved heat transfer performance. The lowest NHFR in the PS endwall passage can be attributed to a negatively impactful performance regarding HTC due to an increase in SF MFR, but still allows upstream coolant to adequately cover the region to

ultimately improve endwall heat transfer. The region with the lowest NHFR is seen in the region where the PLV augments into the PV where it is near 0. Even though coolant is present, the baseline case enhanced the strength of the PV enough to almost negate the benefits of coolant.

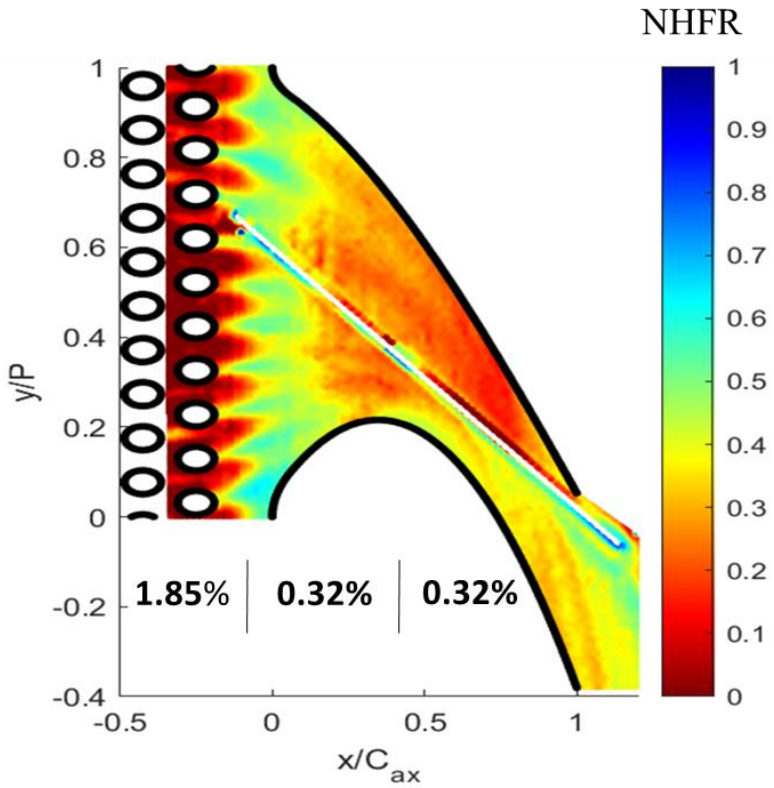

Figure 21. Net heat flux reduction distribution results for baseline case

Another region of interest is the SS endwall near the throat. Both the egression vortex and stagnation point drastically improve local net heat flux by diverting upstream coolant to these areas. The SS endwall region in general reduces heat transfer by 35%. The SF gap diminishes the secondary flow enough as well as diverting upstream coolant adequately to the SS endwall that significant improvements are still observed with the least optimal case. However, further upstream above the vane SS apex lies a region of low NHFR. Although this region does receive ample film cooling, the changes in the endwall flow interaction with the slashface gap experienced with high SF MFR nearly negates the added benefits of upstream coolant.

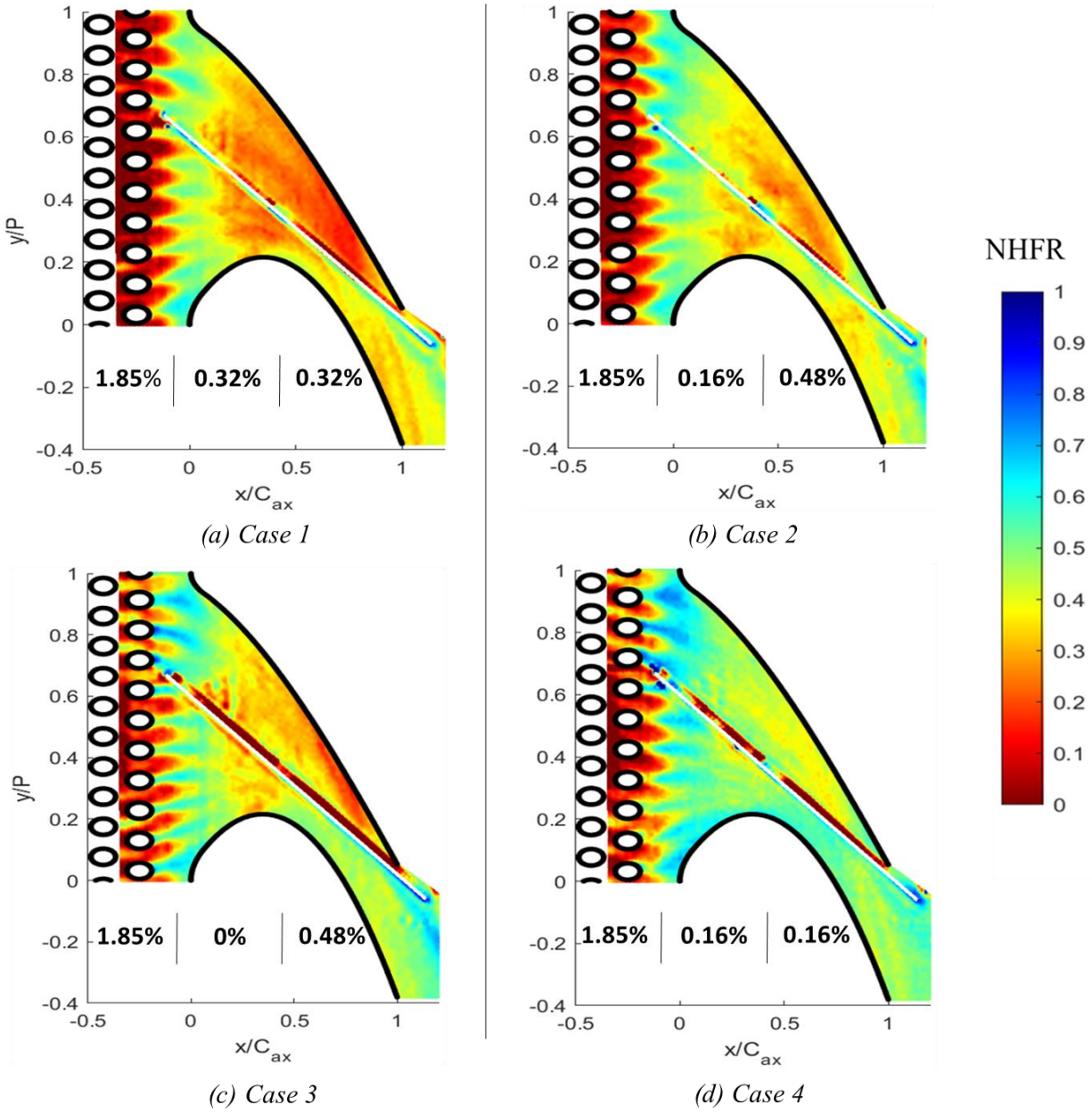

(a) Case 1 *(b) Case 2*

(c) Case 3 *(d) Case 4*

Figure 22. Net heat flux reduction distribution for all reported test cases

Applying the concepts discussed in η and HTC distributions, the most desirable SF MFR configurations are those which minimizes the MFR. One could argue that increasing SF MFR, especially the Fwd cavity MFR, has a direct correlation with increasing the strength of secondary flows throughout the passage. Case 2 supports the significance in the Fwd cavity's role in the development in secondary flows. As half of the Fwd cavity's MFR is shifted to the Aft cavity, compared to the baseline, the development of the SLV and the PV around the SF gap reveals a

significant decrease in adverse heat transfer effects. The corner vortex seen at the PS TE also appears to be mitigated with a significant reduction in heat transfer without the need of film cooling penetration.

However, further reduction of the Fwd cavity MFR to 0% shown in case 3 signals a more unbalanced ingestion and egression behavior that impairs the development of secondary flows for an improved coolant environment. Case 4 presents the configuration with the largest improvements in convective heat transfer parameters. This case is defined as improving all areas of the passage, including the PS TE region, in terms of reducing the net amount of heat flux entering the endwall. Not only does this case provide the most improved environment for endwall film cooling, it also uses the least resources to do so. Nevertheless, because of the lack of variety in η distributions in all test cases that lie within experimental uncertainty, no case can be definitively distinguished as the best performance. Even then, patterns of HTC distributions that are distinguished outside of experimental uncertainty can lead to the general observation that lower SF MFR provides an improved environment for endwall film cooling.

F. CFD: Dual vs Single Cavity

A numerical simulation is employed using the two following cavity configurations displayed in Figure 23. The primary geometry under investigation showcases two individual cavities providing coolant into the forward and aft portion of the slashface gap. The single cavity extends the dual cavity to a single cavity for evaluating the effectiveness of the dual cavity compared to a typical, single cavity configuration. This study is limited in resources to experimentally test another article, and the lack of literature in dual cavity performance warranted a computational investigation. Coolant is injected at the position of the seal slot (yellow/blue surfaces) to imitate the strip seal in CFD. Following experimental nomenclature, the cavities will also be referred to as plenums. The mass flow ratios for the dual-plenum case are MFR_{fwd} = 0.32%, MFR_{aft} = 0.32%, and MFR_{sing} = 0.64% for the single plenum case. The MFR of the jump cooling cavity remains 1.85%.

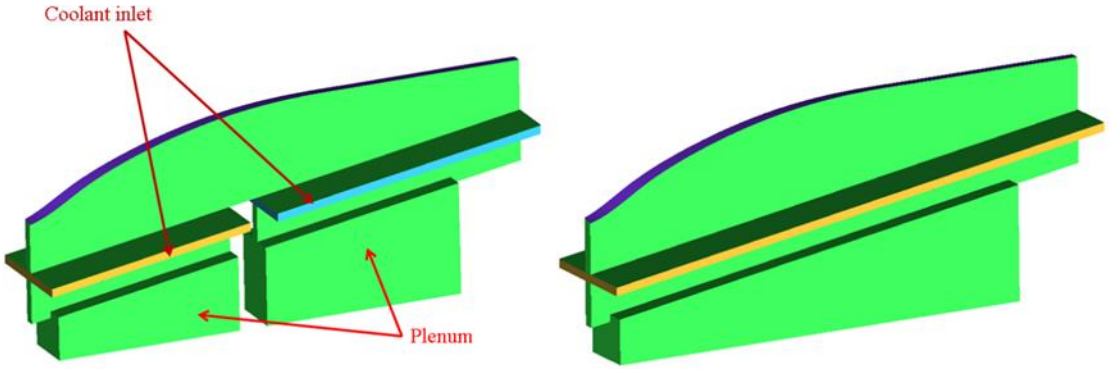

(a) Dual plenum *(b) Single plenum*

Figure 23. Computational geometry of each slashface plenum configuration

The resulting endwall film cooling effectiveness (η) and heat transfer coefficient (HTC) distributions are presented in Figures 24 and 25, respectively. Replacing the dual slashface cavity with a large single cavity details the most significant changes in coolant coverage and heat transfer levels are observed downstream of the slashface trailing edge. Another difference in terms of η is shown on the pressure side endwall along the slashface gap. In this area, averaged film cooling effectiveness is further decreased from 0.2 to 0 after adopting the single cavity. For the other regions of the endwall, the η distribution is primarily a result of the upstream jump cooling instead of slashface leakage and is influenced slightly in terms of increased film cooling effectiveness throughout when using the dual cavity slashface.

The coolant coverage resulting from the egression vortex becomes much shorter but slightly wider for the single cavity case. Coolant coverage in this region is strengthened as more coolant is ingested and ejected. However, the larger momentum in reattachment does not perform well effectively distributing coolant coverage downstream as seen with the dual cavity configuration. HTC in this region is correspondingly enhanced when adopting the single slashface plenum due to the turbulent nature of reattachment. A narrow band of high HTC also appears between $0<x/C_{ax}<0.7$ along the gap interface towards PS for the single plenum case. This can be attributed to the changes in the flow interaction with the slashface gap where the single cavity configuration shows ingestion into the gap from the PS that is elongated throughout the passage until the passage vortex (PV) cross overs the gap.

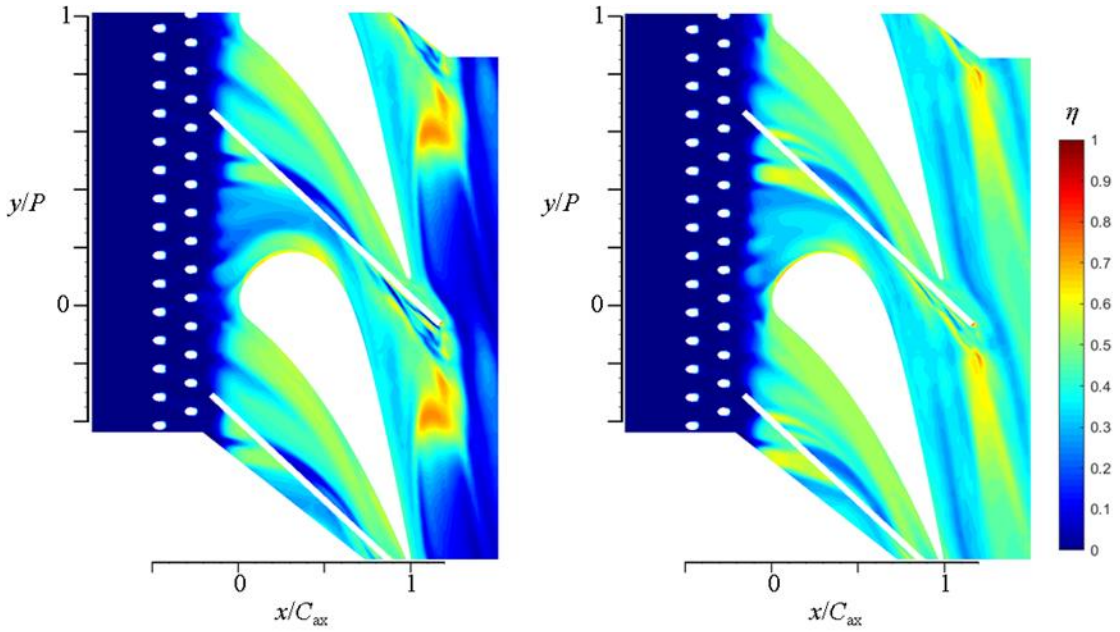

(a) Single cavity *(b) Dual cavity*

Figure 24. CFD comparison of endwall adiabatic film cooling effectiveness distribution

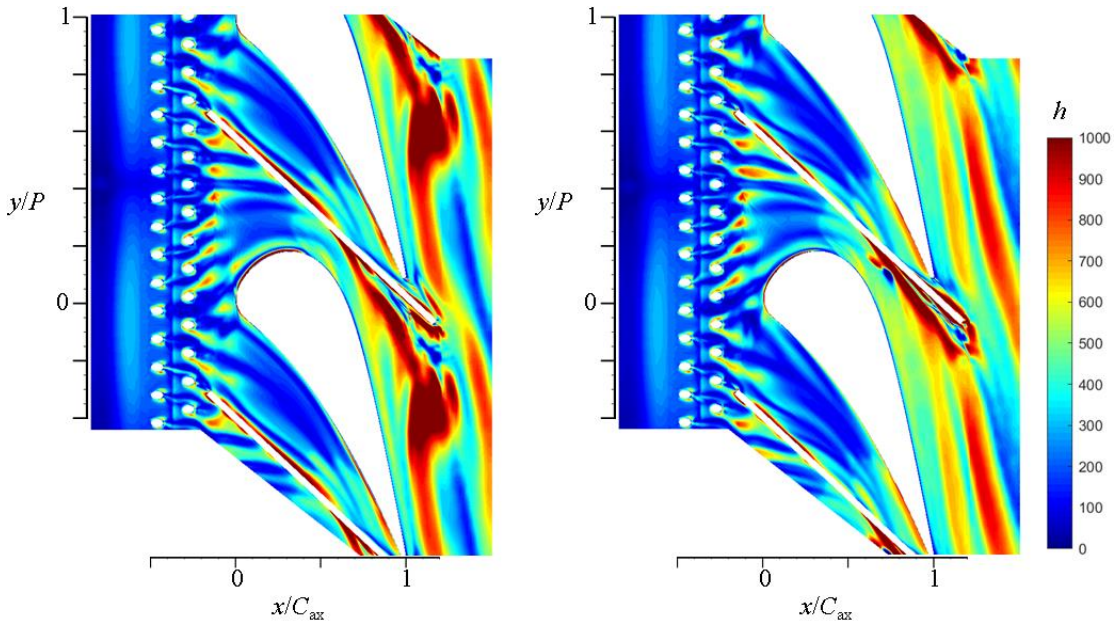

(a) Single cavity *(b) Dual cavity*

Figure 25. CFD comparison of endwall HTC distribution

Comparing the SS endwall shows a general improvement in HTC for the dual cavity. The large, intense region found from the single cavity at the egression vortex reattachment is

diminished when using dual cavities. General egression along the gap towards the SS also has an increased distance of travel before reattaching on the endwall with higher turbulence intensity. This departing egression leaves a much larger area that is exposed to mainstream hot gas that is not seen as significantly in the dual cavity case. These changes in patterns can be best explained by the change in behavior of the slashface gap regarding ingestion and egression.

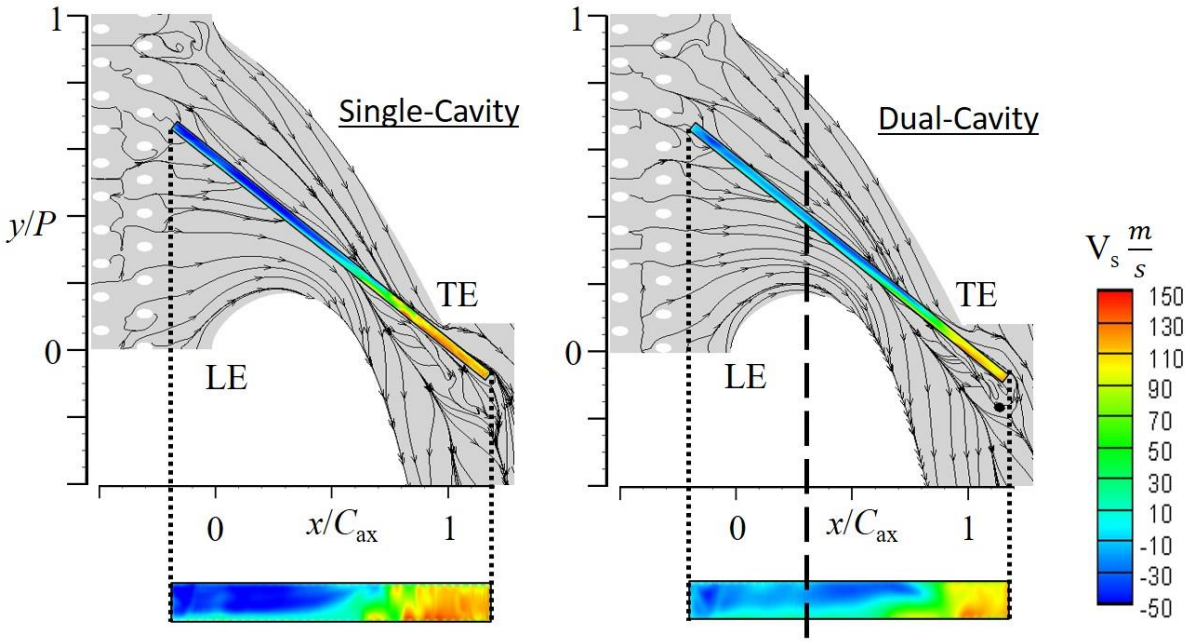

Figure 26. CFD comparison of spanwise velocity along the slashface gap

The spanwise velocity distribution along the slashface gap interface is again shown but with the single cavity counterpoint. The patterns of ingestion and egression show significant differences. The dual cavity sees little ingestion towards the LE and cross flow from SS endwall towards PS endwall. This cross flow can be seen from the CFD η distribution as well as explain the retention of coolant coverage on the PS in the case 4 experimental η distribution (SF MFR: 0.16%, 0.16%). Flow crossing the gap in the Fwd cavity portion of the passage is distinctive in a dual cavity configuration. The single cavity configuration experiences ingestion on a far greater scale and is dominated by PS endwall flow ingestion. Endwall flow ingestion from the PS endwall can explain the narrow band heightened HTC along the gap as the endwall boundary layer thins as well as a reduction in coolant coverage compared to a dual cavity configuration.

Due to this increase in mass flux of ingestion along with conservation of mass, the resulting egression characteristics are magnified as well. Not only does the internal gas start egression farther upstream, but the magnitude of the velocity is also greater. This behavior assists in explaining the larger distance between egression and endwall reattachment in addition to the increase in reattachment turbulence found in the CFD results. Figure 28 details the average spanwise velocity along the gap.

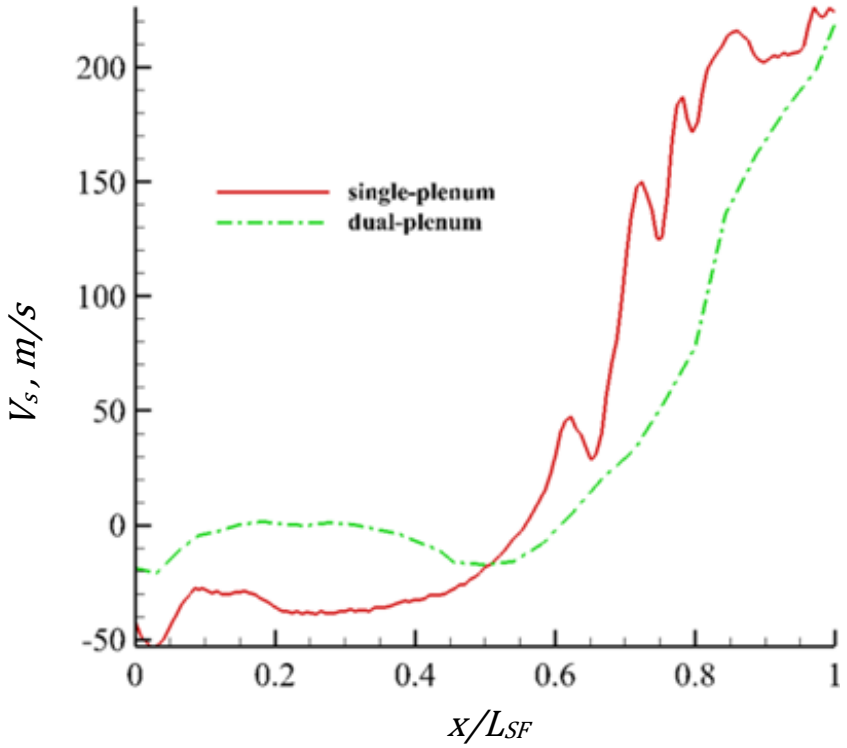

Figure 27. Spanwise velocity of flow along the SF gap interface

The critical difference between the dual cavity and single cavity slashface configuration is the ingestion and egression behavior. From 0 to 0.4 L_{SF} (Fwd Cavity portion), the ingestion flow into the dual plenum is initially high but remains consistent roughly below 0 m/s for the entirety of this portion. As endwall flow meets the Aft cavity of the gap, an abrupt spike in ingestion occurs prior to a gradual increase in egression velocity. Whereas the single cavity maintains a consistent intense ingestion until around the same location (0.4 L_{SF}) where the increase in spanwise velocity is sharp compared to the dual cavity. Both the dual cavity and

single cavity share an inflection in velocity roughly at the same point yet differ in the direction that defines the differences in their response.

The reasoning behind this difference lies within the geometry of the slashface gap wall separating both cavities. As ingested gas travels within the cavity, the gas compresses against the gap wall separating the cavities creating an increased pressure distribution within the portion of the gap. As the blocked flow no longer travels through the entirety of the gap, less mass is transferred in the Aft cavity thus reducing pressure throughout. Figure 28 shows how blocking internal flow increases pressure within the Fwd cavity and reduces pressure in the Aft cavity compared to the single cavity geometry.

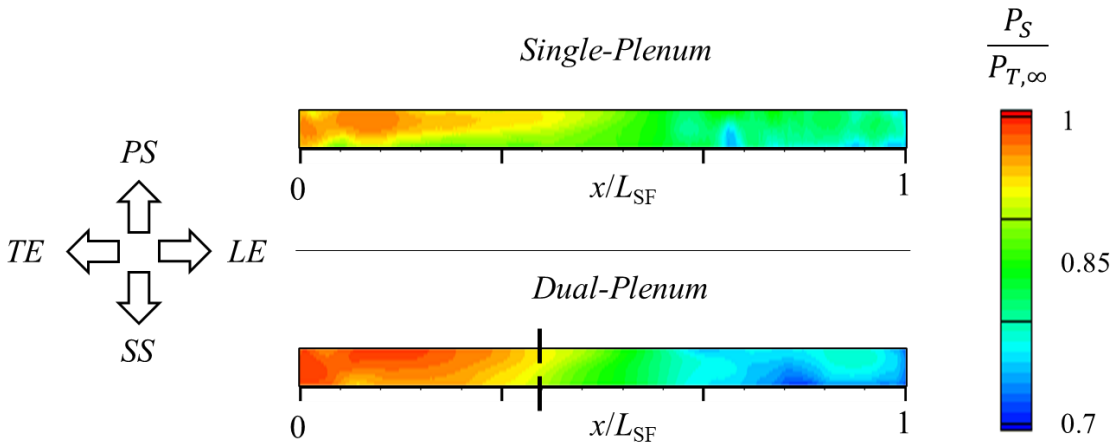

Figure 28. Comparison of pressure along the slashface gap interface normalized to mainstream total pressure

Increasing the pressure further prevents initial high-pressure mainstream flow from ingesting. This prevention of sudden, high momentum ingestion further prevents endwall flow separation when contacting the slashface gap to improve the film cooling environment. The resulting decrease pressure in the Aft cavity has less potential for flow acceleration into the mainstream as the end will encounter mainstream flow of $Ma_{exit} = 0.85$ resulting in a static pressure of 62% of the total pressure. The pressure distribution comparison in the Aft cavity portion in Figure 28 illustrates that the dual cavity is far closer to the mainstream pressure causing far less egression momentum.

The larger range in slashface gap pressure can be attributed as the nature of how dual cavity slashface performs better than a single cavity slashface. The location of the separation

created a more favorable pressure distribution and the resulting spanwise pressure gradients shown in Figure 29 where the span direction goes into the endwall.

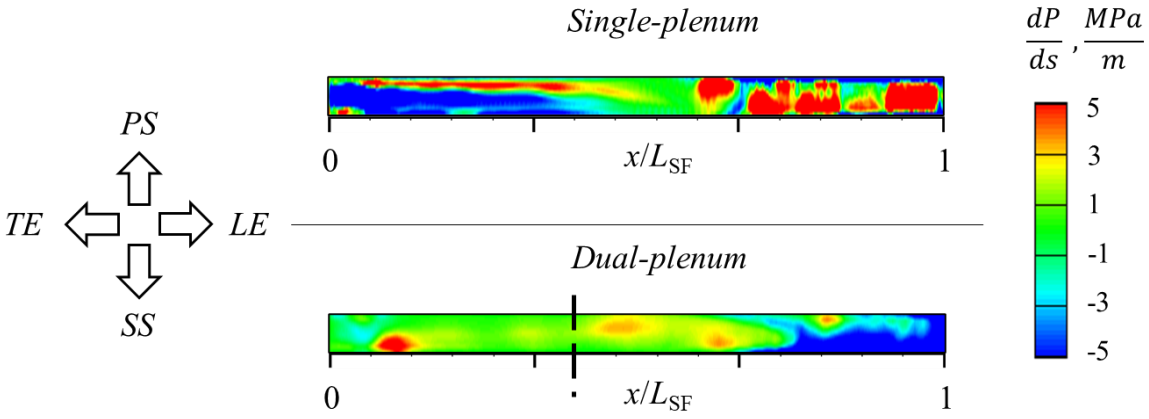

Figure 29. Comparison of spanwise pressure gradient along the slashface gap interface

The single plenum sees drastic changes in the pressure gradient distribution. Initial flow ingestion experiences high deceleration as it confines into the slashface gap. The flow then drastically accelerates as it egresses from the gap reaching actual magnitudes greater than previously presented. Implementing the dual plenum reduces the drastic changes in pressure gradients, and flow egressing from the Aft cavity is immediately decelerated which improves endwall reattachment and general interactions with surrounding flow. Because of the drastic changes in endwall pressure in transonic and other high-speed flow applications, geometry within the passage performs best when taking the pressure gradients into consideration.

Conclusions

The presented investigation sought to test a novel dual cavity slashface gap experimentally and computationally for an application in an NGV endwall operating at transonic high turbulence intensity conditions. The Virginia Tech Transonic Wind Tunnel performed the experimental tests using IR thermography recording transient heat transfer experiments in a quasi-steady state flow field. Heat transfer parameters are analyzed using techniques based upon Cook and Felderman [25] as well as Xue et al. [26]. An experimental oil paint flow visualization

and a CFD study are employed to further understand the physics of slashface gap interaction. The summarized conclusions found are as follows:

1) Compared to a conventional single cavity, a dual cavity slashface gap alters the static pressure distribution closer to the adjacent mainstream pressure along the slashface gap interface. The change in pressure further decelerates the ingested and egressed flow reducing endwall boundary layer thinning and shear interaction in near gap endwall flow.

2) The use of a dual cavity slashface gap increases the pressure drop going downstream along the gap making the geometry more ideal, compared to a single cavity gap, in transonic or other high-speed turbine applications that experiences large mainstream pressure drops as flow accelerates throughout the passage.

3) Altering the slashface coolant MFR results in insignificant changes in endwall adiabatic film cooling effectiveness but provides a first order effect on endwall heat transfer coefficient as endwall flow development is correlated with ingestion and egression flow behavior.

4) Minimizing the slashface coolant MFR proved to have the most positive impact regarding endwall heat transfer as the coefficient magnitude reduced as much as 20% in mid-passage and near throat areas.

The general understanding of the characteristics defining dual cavity slashface cooling is the inherent coupling of upstream coolant and the interaction of the slashface gap with endwall flow in terms of ingestion and egression. Altering these defining characteristics within a set geometry and static upstream coolant can be accomplished by varying SF MFR. Variations of SF MFR varies the pressure distribution within the slashface cavities, and the distribution controls ingestion and egression flow behavior relating to mainstream conditions and the reliant local endwall static pressure throughout the passage. The critical ingestion and egression characteristics which inherently determines the performance of a slashface gap are therefore required to be tested under realistic operating conditions for accurate analysis.

Acknowledgements

The work presented is completed under the industry sponsorship of Hongzhou Xu and Michael Fox of Solar Turbines Incorporated along with the academic guidance of Dr. Wing Ng, Chris C. Kraft Endowed Professor at Virginia Polytechnic Institute and State University. All results from CFD is credited to Kaiyuan Zhang's individual work in a collaborative effort.

References

[1] V.H.S.C. (2002). Stationary flowpath components for gas turbine engine (US6413042B2). U. S. Patent and Trademark Office.

[2] Wang, H. P., Olson, S. J., Goldstein, R. J., & Eckert, E. R. G. (1997). Flow Visualization in a Linear Turbine Cascade of High Performance Turbine Blades. Journal of Turbomachinery, 119(1), 1–8. https://doi.org/10.1115/1.2841006

[3] Aunapu, N. V., Volino, R. J., Flack, K. A., & Stoddard, R. M. (2000). Secondary Flow Measurements in a Turbine Passage With Endwall Flow Modification. Journal of Turbomachinery, 122(4), 651–658. https://doi.org/10.1115/1.1311286

[4] Ames, F. E., Barbot, P. A., & Wang, C. (2003). Effects of Aeroderivative Combustor Turbulence on Endwall Heat Transfer Distributions Acquired in a Linear Vane Cascade. Journal of Turbomachinery, 125(2), 210–220. https://doi.org/10.1115/1.1559897

[5] Blair, M. F. (1974). An Experimental Study of Heat Transfer and Film Cooling on Large-Scale Turbine Endwalls. Journal of Heat Transfer, 96(4), 524–529. https://doi.org/10.1115/1.3450239

[6] Kang, M. B., Kohli, A., & Thole, K. A. (1999). Heat Transfer and Flowfield Measurements in the Leading Edge Region of a Stator Vane Endwall. Journal of Turbomachinery, 121(3), 558–568. https://doi.org/10.1115/1.2841351

[7] Reid, K., Denton, J., Pullan, G., Curtis, E., & Longley, J. (2005). The Interaction of Turbine Inter-Platform Leakage Flow With the Mainstream Flow. Journal of Turbomachinery, 129(2), 303–310. https://doi.org/10.1115/1.2162592

[8] Piggush, J. D., & Simon, T. W. (2012). Flow Measurements in a First Stage Nozzle Cascade Having Endwall Contouring, Leakage, and Assembly Features. Journal of Turbomachinery, 135(1), 1–13. https://doi.org/10.1115/1.4006419

[9] Lynch, S. P., & Thole, K. A. (2011). The Effect of the Combustor-Turbine Slot and Midpassage Gap on Vane Endwall Heat Transfer. Journal of Turbomachinery, 133(4), 1–9. https://doi.org/10.1115/1.4002950

[10] Lynch, S. P., & Thole, K. A. (2017). Heat Transfer and Film Cooling on a Contoured Blade Endwall With Platform Gap Leakage. Journal of Turbomachinery, 139(5), 1–10. https://doi.org/10.1115/1.4035202

[11] Piggush, J. D., & Simon, T. W. (2006). Heat Transfer Measurements in a First-Stage Nozzle Cascade Having Endwall Contouring: Misalignment and Leakage Studies. Journal of Turbomachinery, 129(4), 782–790. https://doi.org/10.1115/1.2720506

[12] Roy, A., Jain, S., Ekkad, S. V., Ng, W., Lohaus, A. S., Crawford, M. E., & Abraham, S. (2017). Heat Transfer Performance of a Transonic Turbine Blade Passage in the Presence of Leakage Flow Through Upstream Slot and Mateface Gap With Endwall Contouring. Journal of Turbomachinery, 139(12), 1–11. https://doi.org/10.1115/1.4037909

[13] Cardwell, N. D., Sundaram, N., & Thole, K. A. (2006). The Effects of Varying the Combustor-Turbine Gap. Journal of Turbomachinery, 129(4), 756–764. https://doi.org/10.1115/1.2720497

[14] Chowdhury, N. H. K., Shiau, C.-C., Han, J.-C., Zhang, L., & Moon, H.-K. (2017). Turbine Vane Endwall Film Cooling With Slashface Leakage and Discrete Hole Configuration. Journal of Turbomachinery, 139(6), 1–11. https://doi.org/10.1115/1.4035162

[14] Chowdhury, N. H. K., Shiau, C.-C., Han, J.-C., Zhang, L., & Moon, H.-K. (2017). Turbine Vane Endwall Film Cooling With Slashface Leakage and Discrete Hole Configuration. Journal of Turbomachinery, 139(6), 1–11. https://doi.org/10.1115/1.4035162

[15] Ranson, W. W., Thole, K. A., & Cunha, F. J. (2005). Adiabatic Effectiveness Measurements and Predictions of Leakage Flows Along a Blade Endwall. Journal of Turbomachinery, 127(3), 609–618. https://doi.org/10.1115/1.1929809

[16] Chen, A. F., Shiau, C.-C., & Han, J.-C. (2017). Turbine Blade Platform Film Cooling With Fan-Shaped Holes Under Simulated Swirl Purge Flow and Slashface Leakage Conditions. Journal of Turbomachinery, 140(1), 1–10. https://doi.org/10.1115/1.4038150Configuration. Journal of Turbomachinery, 139(6), 1–11. https://doi.org/10.1115/1.4035162

[17] Granser, D. and Schulenberg, T., 1990. "Prediction and Measurement of Film Cooling Effectiveness for a FirstStage Turbine Vane Shroud," ASME paper 90-GT-95.

[18] Zhang, L.J. and R.S. Jaiswal, 2001. "Turbine Nozzle Endwall Film Cooling Study Using Pressure-Sensitive Paint," Transactions of the ASME Journal of Turbomachinery, Vol 123, pp. 730-738.

[19] Sibold, R. (2019). The Effect of Density Ratio on Steep Injection Angle Purge Jet Cooling for a Converging Nozzle Guide Vane Endwall at Transonic Conditions [Unpublished Master's Thesis]. Virginia Polytechnic Institute and State University.

[20] Mayo, D. E., Arisi, A., Ng, W. F., Li, Z., Li, J., Moon, H.-K., and Zhang, L., 2017, "Effect of Combustor-Turbine Platform Misalignment on the Aerodynamics and Heat Transfer of an Axisymmetric Converging Vane Endwall at Transonic Conditions," ASME Turbo Expo: Power and Land, Sea, and Air, ASME, Charlotte, NC, pp. 1–11.

[21] Nasir, S., Carullo, J. S., Ng, W.-F., Thole, K. A., Wu, H., Zhang, L. J., and Moon, H. K., 2009, "Effects of Large Scale High Freestream Turbulence and Exit Reynolds Number on Turbine Vane Heat Transfer in a Transonic Cascade," J. Turbomach., 131(2), pp. 021021-021021–11.

[22] Holmberg, D. G., and Diller, T. E., 2004, "Simultaneous Heat Flux and Velocity Measurements in a Transonic Turbine Cascade," J. Turbomach., 127(3), pp. 502–506.

[23] Nix, A. C., Smith, A. C., Diller, T. E., Ng, W. F., and Thole, K. A., 2002, "High Intensity, Large Length-Scale Freestream Turbulence Generation in a Transonic Cascade," ASME Turbo Expo, ASME, Amserdam, Netherlands, pp. 1–8.

[24] Teekaram, A. J. H., Forth, C. J. P., and Jones, T. V., 1989, "The Use of Foreign Gas to Simulate the Effects of Density Ratios in Film Cooling," J. Turbomach., 111(1), pp. 57–62.

[25] Cook, W. J., and Felderman, E. J., 1966, "Reduction of Data from Thin-Film HeatTransfer Gauges: A Concise Numerical Technique," AIAA J., 4(3), pp. 561–562.

[26] Xue, S., Roy, A., Ng, W. F., and Ekkad, S. V., 2015, "A Novel Transient Technique to Determine Recovery Temperature, Heat Transfer Coefficient, and Film Cooling Effectiveness Simultaneously in a Transonic Turbine Cascade," J. Therm. Sci. Eng. Appl., 7(1), pp. 011016-011016–10.

[27] Li, W., Lu, X., Li, X., Ren, J., and Jiang, H., 2019, "Wall thickness and injection direction effects on flat plate full-coverage film cooling arrays: Adiabatic film effectiveness and heat transfer coefficient," Int. J. Therm. Sci., 136, pp. 172–181.

[28] Sen, B., Schmidt, D. L., and Bogard, D. G., 2010, "Film Cooling With Compound Angle Holes: Heat Transfer," J. Turbomach., 118(4), pp. 800–806.

[29] Mick, W. J., and Mayle, R. E., 1988, "Stagnation Film Cooling and Heat Transfer, Including Its Effect Within the Hole Pattern," J. Turbomach., 110(1), pp. 66–72.

[30] Moffat, R. J., 1988, "Describing the uncertainties in experimental results," Exp. Therm. Fluid Sci., 1(1), pp. 3–17.

[31] Kline, S. J., and McClintock, F. A., 1953, "Describing Uncertainties in Single Sample Experiments," Mech. Eng., pp. 3–8.

Appendix A: Remaining Completed Cases

The following additional test cases are reported in the Appendix for further evidence of conclusions. They are not reported throughout the results section due to the impractical applications of the coolant conditions. However, they serve to help better understand the physics around the slashface gap effects as well as confirming patterns seen in previous studies regarding slashface gap leakage.

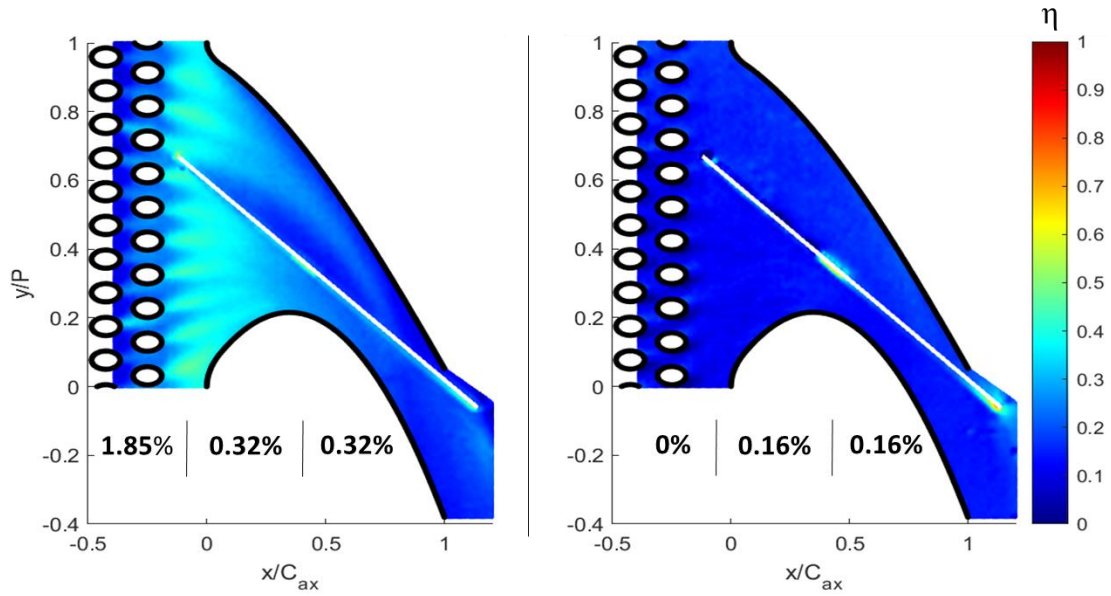

(a) Baseline *(b) Case 5: No JC MFR*

Figure 30. Adiabatic effectiveness distribution comparison between baseline case and no upstream purge coolant

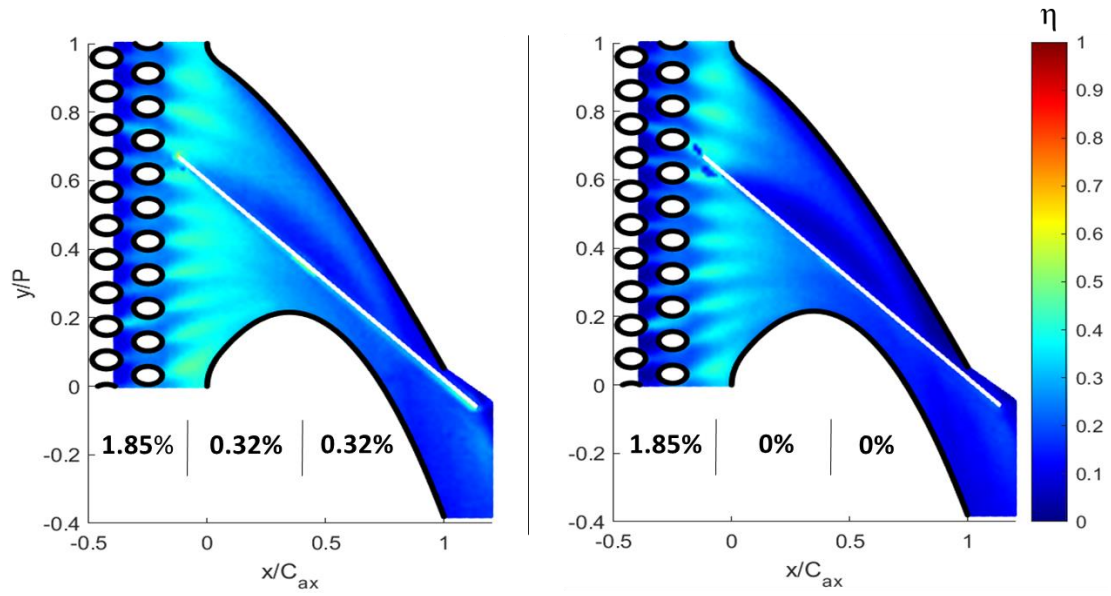

(a) Baseline *(b) Case 6: No SF MFR*

Figure 31. Adiabatic effectiveness distribution comparison between baseline case and no slashface leakage

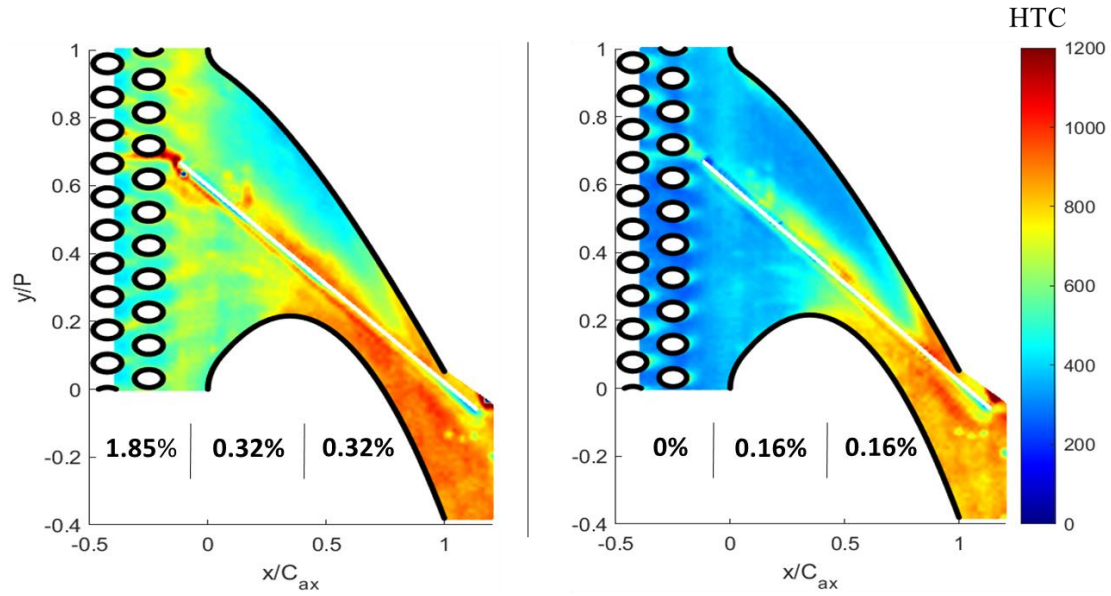

(a) Baseline *(b) Case 5: No JC MFR*

Figure 32. Heat transfer coefficient distribution comparison between baseline case and no upstream purge coolant

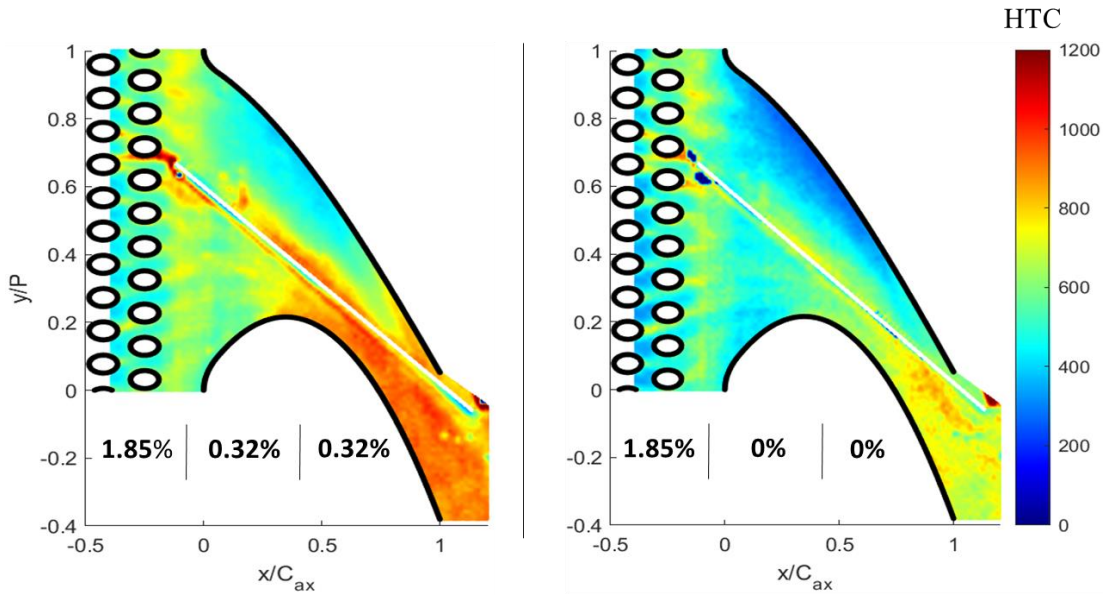

(a) Baseline *(b) Case 6: No SF MFR*

Figure 33. Heat transfer coefficient distribution comparison between baseline case and no slashface leakage

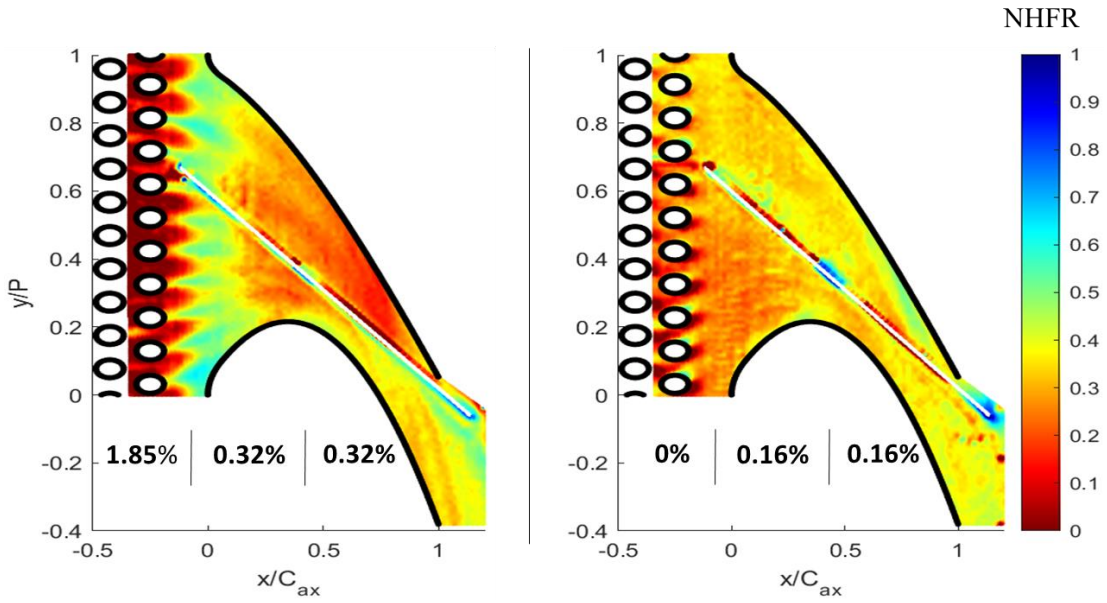

(a) Baseline *(b) Case 5: No JC MFR*

Figure 34. Net heat flux reduction distribution comparison between baseline case and no upstream purge coolant

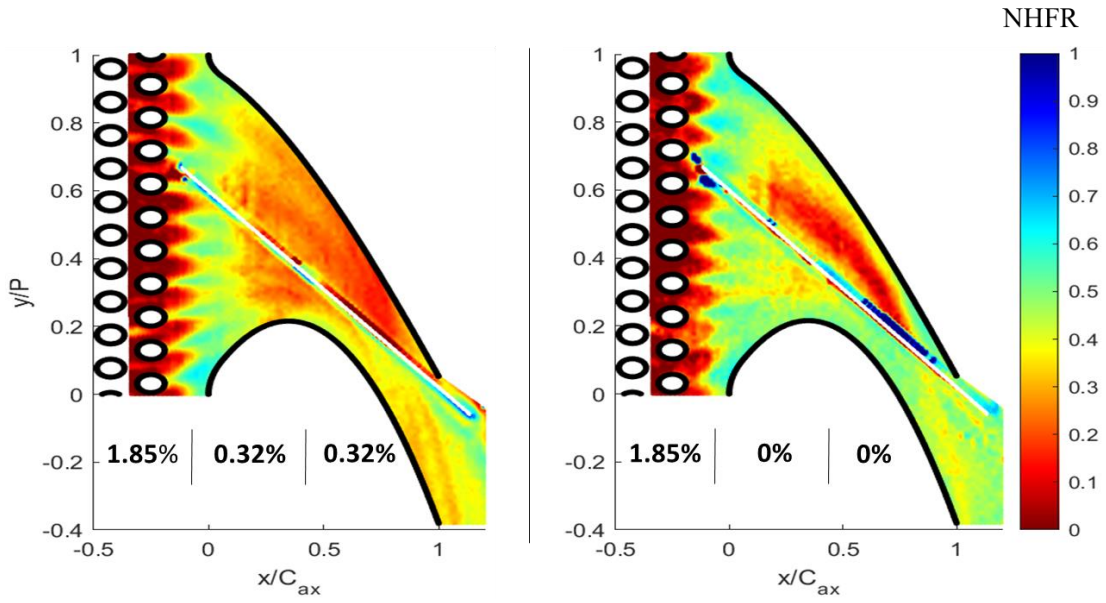

(a) Baseline *(b) Case 6: No SF MFR*

Figure 35. Net heat flux reduction distribution comparison between baseline case and slashface leakage

Appendix B: Mainstream Conditions Calculation

Both inlet and outlet Mach numbers are calculated using experimental pressure measurements. The upstream pitot-static probe gathered the total pressure of the mainstream, and the 6 static ports upstream and the 6 downstream of the passage gathered the static pressure of the mainstream for both inlet and exit calculations, respectively. These pressure measurements are collected for storage using a NetScanner Model 98RK boasting an accuracy of ± 0.05% of the full scale. Then, the pressure measurements are used to calculate the Mach number following Equation 12 to provide real time Mach number estimations seen in Figure 38. The target exit Mach number is 0.85, but a range of ± 5% is allowable as acceptable conditions.

$$Ma = \sqrt{\frac{2}{\gamma - 1}\left(\left(\frac{P_t}{P_s}\right)^{\frac{\gamma-1}{\gamma}} - 1\right)}$$

Equation 12. Mainstream Mach number calculation

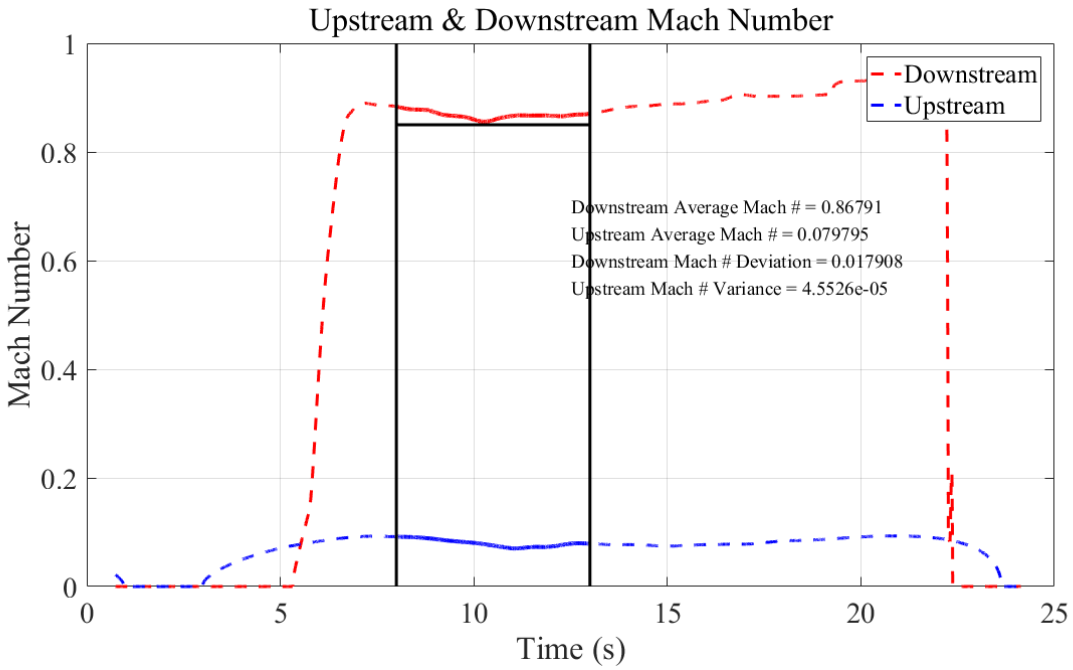

Figure 36. Example of experimental based calculation for mainstream inlet and exit Mach number plot

Appendix C: IR Camera Calibration

Calibrating the FLIR A325sc IR camera is essential to account for error-inducing factors within the experimental setup such as the Germanium window complete lack of transmissivity, slight endwall curvature, endwall roughness, and a lack of complete black-body emissivity from the ultra-flat black paint. Characterizing the camera readings requires a T-type thermocouple mounted at the location on the endwall of the camera reading as a reference temperature. The endwall is then heated using a blow-dryer to a temperature typically found during a heat transfer blowdown experiment. The heat is no longer applied to measure the transient response for both the thermocouple and endwall seen in Figure 39. Peak temperature readings are temporally aligned to ensure the measurements are synchronized.

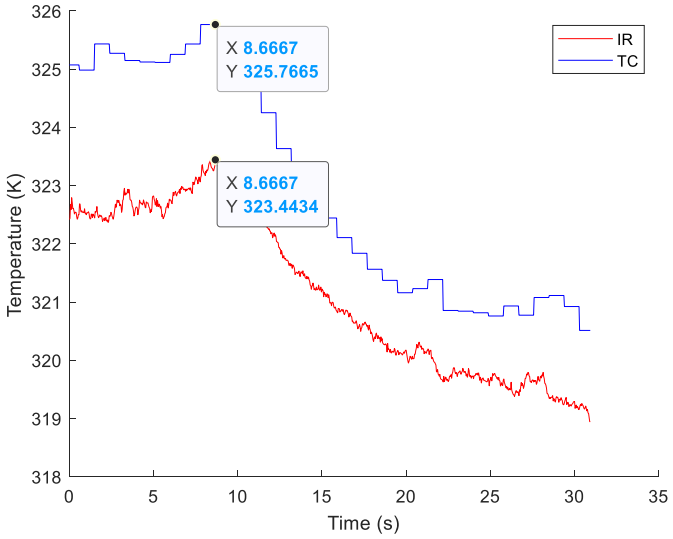

Figure 37. IR camera calibration raw data aligned plot

The transient response is measured for calibration for two reasons: First, the experimental heat transfer measurements are taken at transient states. This is meant to calibrate the camera as if there is a thermocouple reading at each pixel point on the endwall. Second, this provides continuous samples across the temperature range of interest while providing enough data points to conform well in a linear regression analysis. The resulting calibration regression and equation in Figure 40 is then implemented to alter IR temperature readings prior to analysis throughout the study.

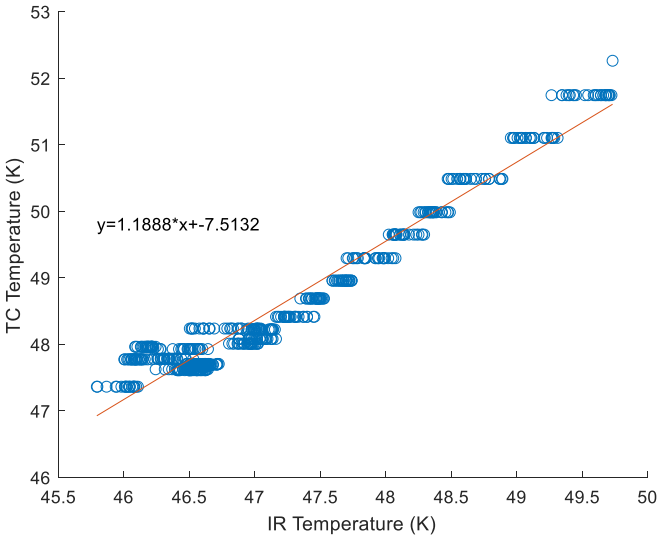

Figure 38. IR camera linear regression plot